Version of Record: https://www.sciencedirect.com/science/article/pii/S0013795221000685
Manuscript_5bd2492c885eff2306ed0e13af45b23b

Microstructural Evolution of Granitic Stones Exposed to Different Thermal Regimes Analysed by Infrared Thermography.

T. Junique[1] • P. Vázquez[1] • Y. Géraud[2]• C. Thomachot-Schneider[1] • H. Sidibé[1]

[1]GEGENAA EA 3795, University of Reims Champagne-Ardenne, 2, esplanade Roland Garros, 51100 Reims, France

[2]GeoRessources Laboratory UMR 7359, University of Lorraine, F54505 Vandoeuvre les Nancy

ABSTRACT

Detailed knowledge of the behaviour of rocks under thermal stress is essential in a variety of fields such as the exploitation of oil and mineral resources, the geothermal sector, the storage of radioactive liquid waste, or even CO_2 capture and storage.

Granites are widely studied and exploited in these fields, and they show different reactions to high-temperature and thermal cycles due mainly to their high mineralogical and textural heterogeneity. One of the features that influences the most the thermal response is the porosity.

The objective of this study is to evaluate the influence of porosity when these rocks are exposed to different thermal treatments. For that purpose, experiments were carried out on four granitoids selected by their similar crystal size, but with variable mineral proportion and porosity values, ranging from 1 to 6%. Two kinds of tests were performed: i) progressive heating cycles from 90 °C to 130 °C to determine the critical threshold for thermal damage; ii) thermal fatigue with cycles of heating-cooling up to 200 °C.

The porosity and the water transport phenomena of the samples were characterised before and after each cycle by the monitoring of capillary water uptake coupled with infrared thermography. This technique allowed to follow the capillary fringe migration during the test and the evolution of the cooling rate index. The direct assessment of the damage was carried out by mercury injection porosimetry, optical polarising microscopy, and scanning electron microscopy.

The combination of all the results permitted to establish a link between the evolution of temperature and the modification of porous networks in granitoids. Microcracks appeared

© 2021 published by Elsevier. This manuscript is made available under the CC BY NC user license
https://creativecommons.org/licenses/by-nc/4.0/

distinctly at a temperature between 90 °C to 130 °C for high porosity granitoids whose Quartz/Feldspar ratio was close to 1. For higher temperatures, the low porosity granitoids develop microcracks from the first heating cycle. The porosity then showed a stronger impact on thermal behaviour than the effect of the mineralogy. The results obtained from infrared thermography allowed to detect the strong variations in the microstructure.

Keywords: Thermal damage; Granites; Critical threshold; Thermal fatigue; Microcracks; Infrared thermography

1_INTRODUCTION

The effect of temperature on rock structures has been widely studied because of its common presence in many geological applications. Examples may be found in the field of ores, hydrocarbons, storage of nuclear waste or CO_2, as well as in the geothermal resources, in which the energy is recovered thanks to the circulation of fluid through its porosity (faults, fractures and matrix) (Bai et al., 2018; Pandey et al., 2017; Parnell, 1988; Witherspoon et al., 1980). In the latter, the injection of cold water into hot rock is used to increase the transfer properties of the neighbouring rocks and causes a slow cooling of the peripheral rock mass (Isaka et al., 2018). These heating and cooling cycles alter the intact rock and thus, influence the fluid flow and in some occasions the stability of the well (Kumari et al., 2017). The temperature of geothermal systems can be low temperature like 80 °C, but the global average temperature is around 200 °C (Breede et al., 2013; Olasolo et al., 2016). Granites are also prospected for geological disposal of radioactive waste, the containers used in deep storage can expose the surrounding rock masses to temperatures likely to degrade the rock microstructure (Chen et al., 2017a). For the storage of high-level radioactive waste, the temperature in the canister surfaces must not exceed 100 °C (Hoekmark and Faelth, 2003). The temperature also has an impact on deep tunnels which can generate thermal stress on rocks surrounding tunnels, most of which do not exceed 130 °C (Chen et al., 2018).

The flow properties and the mechanical strength of the rocks are directly influenced by their microstructures. Recent studies have been conducted at pore-scale to characterise the physical parameters of the rock such as porosity, permeability, or elastic properties for natural strain (Chaki et al., 2008; Staněk and Géraud, 2019). The influence of the temperature is not yet well studied. Unravelling these physical parameters and the

59 microstructures of the rock allows the understanding and the extrapolation to a large-scale
60 system.

61 Granite is a material showing high mechanical strength with low matrix porosity and
62 heterogeneous mineralogy, which makes it also very sensitive to the effects of temperature
63 (Heuze, 1983). The differential mineral dilation, in most cases anisotropic (Berest and
64 Vouille, 1988; Vázquez et al., 2011) may develop a microcracking (intergranular and
65 intragranular) from a certain temperature threshold (Géraud et al., 1992). This critical
66 temperature generates significant changes in physical properties. In general, microscopic
67 observations show that microcracking often follows preferential directions, such as cleavage
68 planes and crystal boundaries in rocks with pre-existing microcracks, because less energy is
69 needed to generate microcracking (Gómez-Heras et al., 2006). The ratio Quartz/Feldspar
70 (Qz/F) plays a determinant role in the microstress development, and consequently in the
71 decay of granite (Sajid and Arif, 2015; Sousa, 2013; Tuğrul and Zarif, 1999; Vázquez et al.,
72 2015).

73 During heating procedures with gradual temperatures, most of the studies conclude that the
74 temperature threshold corresponding to the beginning of microcracks development is about
75 120-130 °C (Darot et al., 1992; Guo et al., 2018; Lin, 2002). Geothermal systems operate on
76 the principle of repetition of heating-cooling, and consequently, it becomes crucial to control
77 the influence of the fatigue on the microstructure of the rock. In general, thermal fatigue in
78 rocks leads to the propagation of pre-existing microcracks over cycling. Few works were
79 done on the influence of fatigue thermal cycles on granite structures (Freire-Lista et al.,
80 2016; Lin, 2002).

81 The main objective of this study is to assess the evolution of the granite pore network when
82 these rocks are exposed in a geothermal system. Works on the thermal effects in relatively
83 low geothermal temperature ranges (<200 °C) is scarce, as well as on damage during its long-
84 term operation period. For that purpose, four granites, with similar mineralogy and crystal
85 size but with different porosity values that ranged from 1 to 6%, were tested. Two different
86 experiments were performed to determine the rock microcrack threshold by progressive
87 heating cycles from 90 °C to 130 °C (EXP1) and to evaluate the thermal fatigue after five
88 cycles at 200 °C (EXP2).

The samples were characterised in their healthy state and after each experiment by destructive and non-destructive methods such as Capillary Water Uptake Tests (CWUT), Infrared Thermography (IRT) monitoring, Mercury Injection Porosimetry (MIP), Optical Polarising Microscopy (POL), and Scanning Electron Microscopy (SEM).

2_MATERIALS

2.1 Geological settings

Four types of granite were chosen due to their similar mineralogy and crystal size but their difference in alteration degree and consequently in porosity. Their commercial names are Albero (A), Gris Alba (GA), Golden Ski (GS), and Silvestre Moreno (SM). They all come from the Iberian peninsula. The orientation of the (XYZ) axes was defined by the main crack system and the orientation of the mica plane in the quarry (Vázquez et al., 2011).

The four studied granites belong to the group of peraluminous syn- and post-kinematic granites. This group includes granites temporally related to processes of Hercynian crustal anatexis (Farias et al., 1987; Vera, 2004).

2.2 Granite description

The studied granites are shown in figure 1, their main petrographic characteristics are introduced in table 1. The petrographic characterisation (mineral proportion) was made with POL and crystal size was measured on the photographs at the macroscopic scale (Vázquez et al., 2018).

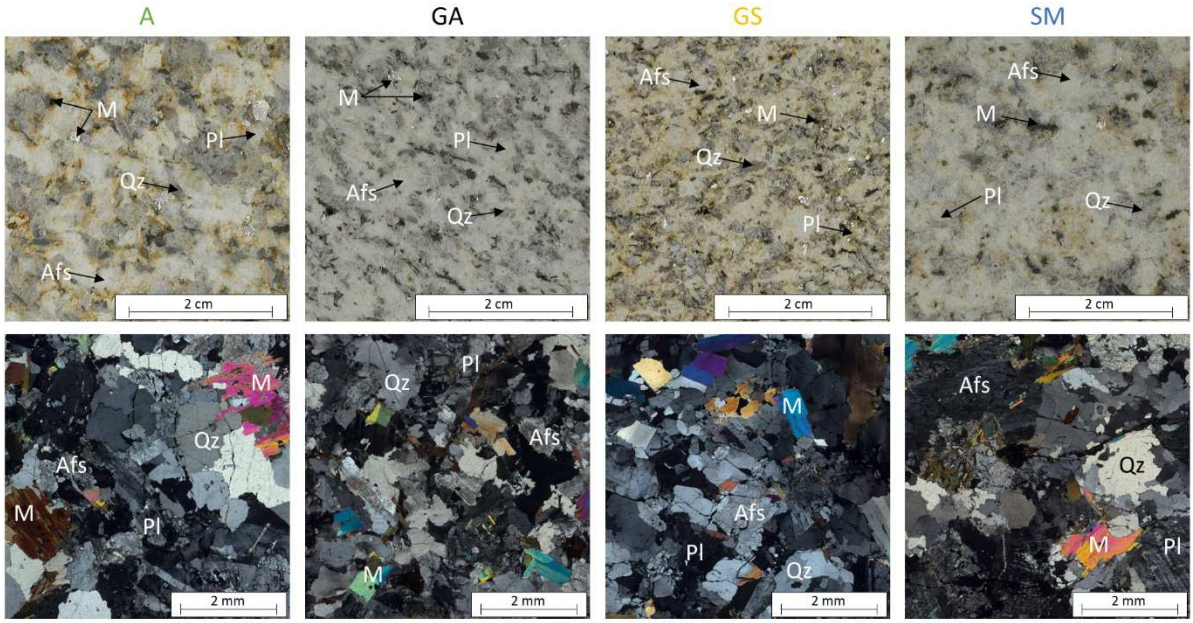

Figure 1: Macroscopic and microscopic photographs (Polarised light optical microscopy) of the studied granite: Albero (A); Gris Alba (GA); Golden Ski (GS); Silvestre Moreno (SM). (Qz: quartz; Afs: alkali feldspar; Pl: plagioclase; M: mica).

Table 1: Main characteristics of the selected granitoids: Trade name, Mineral proportion, IUGS classification (Le Maitre, 2002), Qz/F ratio (Qz: Quartz; F: Alkali feldspar + Plagioclase) and crystal size (Vázquez et al., 2018).

Granite	Composition (%)						Macroscopical crystal size (mm)				
	Qz	Afs	Pl	M	IUGS classification	Qz/F ratio	Qz	Afs	Pl	M	Average
A (Albero)	35	10	30	25	Granodiorite	0.88	5	5	6	4	5
GA (Gris Alba)	23	37	23	17	Monzogranite	0.37	5	5	4	2	4
GS (Golden Ski)	47	20	20	13	Monzogranite	1.18	4	4	4	2	4
SM (Silvestre Moreno)	45	20	20	15	Monzogranite	1.13	4	5	7	4	5

Qz: quartz; Afs: alkali feldspar; Pl: plagioclase; M: mica.

Albero (A): It is a homogeneous granodiorite with medium-fine crystal size (5 mm). It has the lowest alkali feldspar content among the four granites studied and a high proportion of mica (25%) with a similar proportion of muscovite and biotite. This granitoid is characterised by open transgranular microcracks.

Gris Alba (GA): It is a homogeneous monzogranite with a fine crystal size (4 mm). It has anhedral minerals and the boundaries between the quartz crystals are irregular. The proportion of muscovite/biotite minerals is about 2:1. The intergranular microcracks observed in this granite are located at the mica edges.

Golden Ski (GS): It is a homogeneous monzogranite with a fine crystal size (4 mm). Quartz and feldspars are subhedral and muscovite is euhedral. The muscovite has the largest crystal size and plagioclase the smallest. Its quartz content is higher than that of feldspars. Pre-existing microcracks are intergranular and are present in plagioclases. GS also has open transgranular microcracks.

Silvestre Moreno (SM): It is a homogeneous fine sized monzogranite (5 mm). These minerals are subidiomorphic. After GS, this granite has the highest quartz proportion of the granitoids studied and proportions of feldspars and plagioclase are similar (20%). Plagioclases are the minerals with the largest size (up to 7 mm). As with A and GS, this granite has an initial alteration highlighted by intra-, inter- and trans-granular microcracks (Vazquez et al., 2018).

An important parameter regarding the mineralogy is the Qz/F ratio. GA has a ratio Qz/F < 0.5, namely a granite rich in feldspar. Meanwhile, A, GS and SM have a similar proportion of both mineral types with values between 0.88 and 1.18. Porosity is the main differencing parameter between these rocks. GA is considered as a fresh granite (porosity <2%, (Vázquez et al., 2018)), with a grey pale colour. The granites A, GS, and SM show a yellow colour that indicates the presence of clays due to previous weathering and consequently a higher voids volume than the fresh rock. These three granites exhibit large intra-, inter-, and trans-granular microcracks, giving them high water porosity for the granite range as well as high capillary transfer.

3_METHODOLOGY

3.1 Heating set up

Two types of heating-cooling tests (EXP1 and EXP2) were performed on 2 samples of each granite with a rectangular prism shape of 10 mm × 40 mm × 40 mm in dimension. In addition, smaller samples of 10 mm × 10 mm × 15 mm (8 samples per granite type for EXP1 and 3 samples per granite type for EXP2) were also tested at the same time for further destructive analyses as MIP (Ritter and Drake, 1945), SEM (Fan et al., 2017). Two thin sections per granite were produced in the initial state and after heating to 200 °C for observations under POL (Freire-Lista et al., 2016; Jin et al., 2019).

- EXP1: this test was conceived to determine the microcrack threshold of each granite. For this aim, 5 cycles of heating-cooling at an increasing temperature of 90 °C, 100 °C, 110 °C, 120 °C and 130 °C were undertaken. A climatic chamber "Vötsch VC3" ensured a low heating and cooling rate of 1 °C.min^{-1} to avoid the microcracks formation due to a high-temperature gradient within the sample (Chaki et al., 2008; Dwivedi et al., 2008; Homand-Etienne and Houpert, 1989; Reuschlé et al., 2006; Takarli and Prince-Agbodjan, 2008). The target temperature was maintained for 2 hours to assure that the whole sample was completely heated with homogeneous temperature distribution (Chaki et al., 2008; Kumari et al., 2017; Yin et al., 2015). It has been shown that heating time is also an important aspect of the consequences of the heat treatment. The longer temperature duration in the treatment, the greater the damage, but it is emphasised that the main thermal damage occurs within the first 2 hours (Tang et al., 2019). The microstructure evolution was assessed by CWUT and MIP after each cycle, SEM observations were also done at the initial and the final states.

- EXP2: this second test aimed at knowing the effect of the thermal fatigue in microcracked rocks. For this purpose, a repetition of 5 heating cycles up to 200 °C was performed. The heating process was carried out with a muffle furnace "Thermo scientific led M 110" with a heating gradient of 5 °C.min^{-1} to promote microcracking (Ding et al., 2016; Huang et al., 2017; Kumari et al., 2017; Li et al., 2019; Shao et al., 2015). The samples were thermally stabilised after 2 hours at 200 °C. For cooling, the specimens were left in the furnace to undergo slow cooling at a rate of 0.5-1 °C.min^{-1}. CWUT was monitored by IRT after every cycle on one of the samples. SEM and POL observations were carried out on fresh rocks and after the first cycle (200(1) °C).

The different cycles will be designated by the reference (Ref.) given in table 2. The two size categories are represented by the red and green samples. From now on, the followed sample (red) will be called by the abbreviation of the granite (x), the corresponding experience, and the number of the sample (a), i.e x-EXPX(a).

Table 2: Specification of the measurement conditions for samples subjected to the two-heat treatments (EXP1 and EXP2). The red samples were used continuously through each EXP, while the green ones were used only once, as the techniques used were destructive.

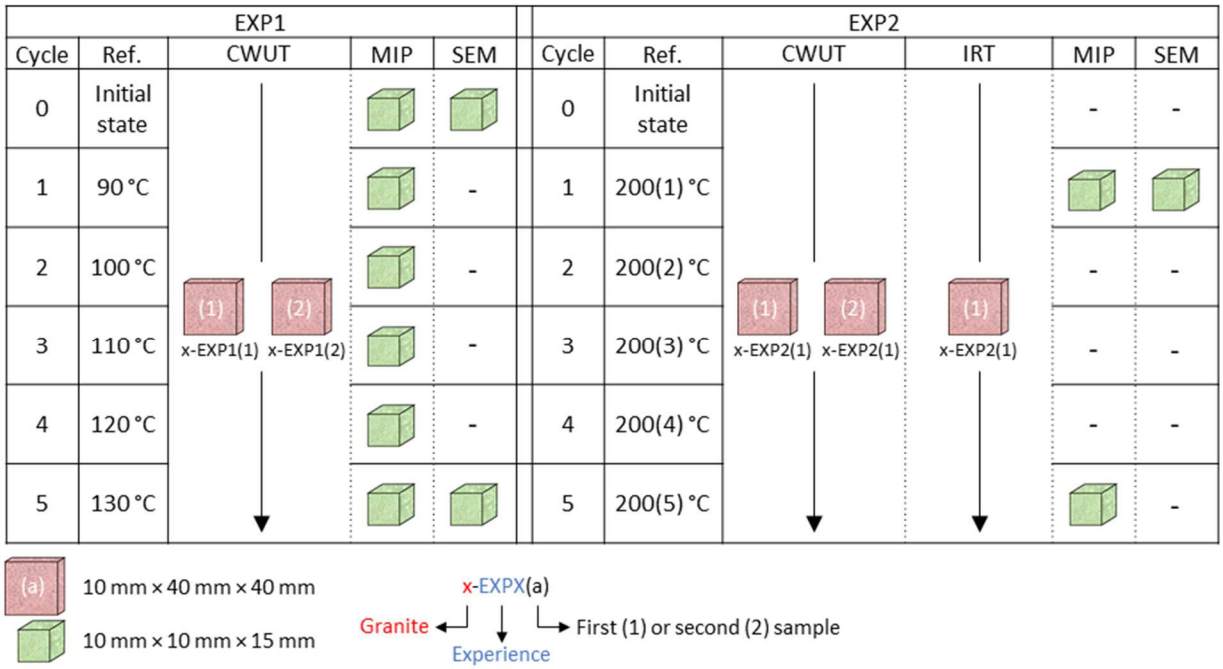

Ref.: reference; CWUT: capillary water uptake tests; MIP: mercury injection porosimetry; SEM: scanning electron microscopy; IRT: infrared thermography.

3.2 Evaluation methods

Microstructural characteristics have been evaluated on the fresh rocks and the samples after heating as described in table 2.

MIP was undertaken before and after the experiments with a Micromeritics Autopore IV 9500 on samples of 10 mm × 10 mm × 15 mm size: one sample per cycle and granite for EXP1 and one sample per granite after one and 5 cycles (200(1) °C and 200(5) °C) for EXP2. Thus, a total of 32 samples were measured. Mercury injection pressures ranged from 0.004 to 228 MPa, giving corresponding pore access radii of 180 to 0.003 µm, respectively.

A total of 12 samples were cut with an approximate size of 10 mm × 10 mm × 15 mm to be tested and studied directly under SEM to avoid the creation of additional microcracks from sawing after the heating. Observations under POL (Olympus BX51) and SEM (Hitachi TM-1000) were done on each granite and after being tested at 130 and 200(1) °C.

3.2.1 Capillary water uptake tests (CWUT) and infrared thermography (IRT) monitoring experimental setup

For both experiments, capillary kinetics were measured on samples after each cycle to assess the modifications of the porous network due to thermal stresses. The capillary

coefficient (C) was calculated based on the NF EN 15801 (2010) standard. After each heating cycle, the granites were thermally stabilised at 40 °C for 2h. Then, the samples were extracted from the climatic chamber and immediately submitted to a capillarity test with water at 23 ± 1 °C, for both experiments. These tests were performed on two samples of each granite with dimensions of 10 mm × 40 mm × 40 mm and the same samples were used for every cycle within the same experience. The samples were suspended from an electronic precision balance, with a readability of 0.1 mg, using a hook and put into contact with distilled water from their bottom face with a fringe of about 1 mm (Fig. 2). The weight was automatically recorded every 10 seconds on a control computer. The temperature of the room was kept at 23 ± 1 °C. The test was carried out for 1 hour, time enough for all the granites to reach the stabilisation of the water uptake. Capillary kinetics are usually characterised by two phases (Hammecker et al., 1993; Hammecker and Jeannette, 1994). The first phase is the progressive filling of the free porosity by the capillary forces of the water without external pressure applied. The slope of this curve that corresponds to the coefficient C ($g.m^{-2}.s^{-1/2}$) (Roels et al., 2000) and depends on the porous network. The second phase, slower, begins after the break of slope and corresponds to the filling of the porous network by diffusion of water in the air.

The coefficient C was calculated for each sample, per cycle, to assess the water kinetic evolution and consequently the variations in the porous network. This test was carried out in two samples to verify the repeatability. For heterogeneous rocks with low porosity, the coefficients evolution of the two samples of each granite assessed individually were more relevant than an average and standard deviation to avoid smoothing of the mean and no longer perceive the changes.

Only for EXP2, IRT monitoring was used to evaluate the microcracking simultaneously to CWUT (Fig. 2). The IRT camera used is a FLIR SC655, operating in wavelengths between 7.5 and 14 µm. The detection temperature of the camera is comprised between -40 and 150 °C with a sensitivity of 0.1 °C. The detector is an uncooled array of microbolometers. The used IRT camera can build images using infrared radiation. The image size is 640 × 480 pixels, with a noise signal of about 40 mK. The recorded signal, called thermosignal (TS), depends on temperature and emissivity and is expressed in isothermal units (IU).

The cooling kinetics of the samples from 40 °C to room temperature was followed by IRT after each heating cycle. The thermal images show that the water spreading into the microstructure and propagating according to the physical characteristics of the material, leading to a possible evaluation of the porosity (Ludwig et al., 2018). The bottom part of the sample was cooled by the water rising by capillarity. The upper part of the sample was not affected by the capillary forces and was used to monitor the cooling by the air.

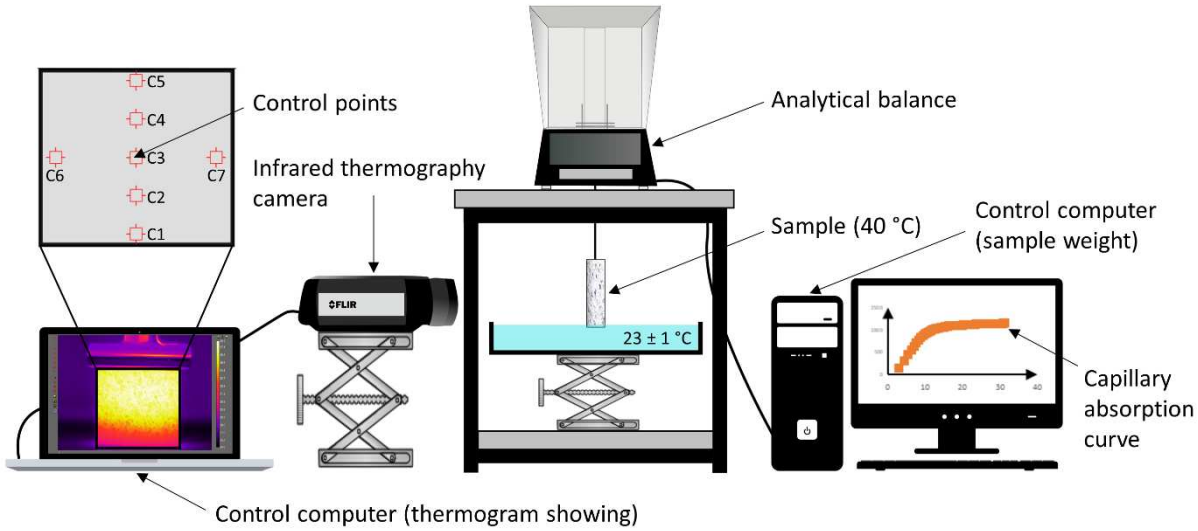

Figure 2: Experimental setup of infrared thermography (IRT) monitoring of a sample submitted to capillary absorption.

The temperature contrast between the rock and the water facilitated the IRT image assessment. This procedure made it possible to observe the progress of the water on the different samples since the rise of the water caused a cooling of the rock and different emissivity of the two media. In the experimental setup, the risks associated with the environmental variations were minimised. The temperature and humidity were monitored with a thermometer and a hygrometer. The experimental device was placed in a watertight tank which allowed to minimise evaporation phenomena as much as possible. Tests were performed in the darkness without artificial light.

The IRT camera was configured to record the thermal images at a rate of 1 frame every 10 seconds for 30 minutes and was activated 1 minute after the start of the experiment to avoid the wide signal variations during the calibrations due to the initial setup. Each image or thermogram of the whole face of each sample acquired during the experiment was processed by the FLIR RESEARCHIR software®. Each pixel of this thermogram corresponds to

a specific temperature value. The interface allows placing control spots of 3 × 3 pixels on the thermogram (C1 to C7, Fig. 2). Five monitoring spots were placed vertically on the sample area, spaced 8 mm. Two spots were placed on the left and right side, centred vertically to observe the possible lateral variations. The "Temporal Plot" function allows us to have the evolution of the thermo-signal as a function of the acquisition time for each control spot.

To quantify the cooling rate, we used the cooling rate index (CRI) representing the temperature variation per unit of time. The CRI10 (calculated for the first 10 minutes of the test) was calculated according to the equation (1) on the 7 control spots of the thermograms and at each cycle. CRI10 index was described for the first time by Pappalardo et al. (2016) in the survey of rock masses as a reliable and best-suited index for the indirect quantification of porosity. According to Mineo and Pappalardo (2016), the cooling curves of a rock show their major evolution during the first 10 minutes, so that this interval was the one chosen for the CRI analysis. This parameter is inspired by Newton's law of cooling, which states that the heat loss of a body is proportional to the temperature difference between the sample and the environment. This law confirms that cooling is faster in the first minutes of the experiment due to the higher temperature difference between the sample and the air or the water. A fractured rock would cool down faster than a non-fractured one. Thus, this index allows to compare the temperature variation as a function of time of the 4 granites during heat treatment cycles and indirectly the microcrack evolution.

$$CRI10 = \Delta T/\Delta t = (T10-T0)/(t10-t0) \quad (1)$$

Where ΔT is the variation in temperature between initial temperature (T0) and temperature after 10 minutes (T10) and Δt is the duration between the two temperature values, i.e. 10 min. High CRI10 values corresponded to a fast cooling and higher cracking than low values that represented a slow cooling.

The low porosity of the granites together with the evaporation and the air-environment makes it difficult to distinguish accurately the water limit of the capillary fringe with the naked eye and on the IRT images. The SURFER software® was used to facilitate the visualisation of the CRI10 and the capillary fringe on the surface of the samples. This software transformed the CRI10 data on grids in 2D by, in this case, the kriging method. Figure 3a shows the schematic distribution of CRI10 on the surface of a sample. The X and Y

axes of the grids represented the dimensions of the sample in centimetres. For a time-lapse of 10 min, the placement of the isolines made it possible to detect the thermal contrast between wet and dry areas.

It has been considered 2 heat transfers: the air cooling and the water cooling. In both cases, the sample was at a temperature of 40 °C and the water and air about 20 °C lower.

- The air cooling on the top of the sample was quantified thanks to the C5 spot (the highest on the sample). Within the 10-minute time-lapse the capillary fringe of the water was not able to reach the C5 spot so that it did not influence the natural cooling of the rock at this point. In addition, this control spot was the closest to the upper surface, in which the temperature equilibrium was reached faster. Thus, the CRI10 (C5) values corresponded to the air-cooling velocity of the rock.
- The water cooling of the bottom of the sample was produced by CWUT. The bottom part showed slower cooling rates than the upper part due to its fast temperature decrease during the first-minute contact with the water. The diffusion of water in the sample resulted in isolines of low value, horizontal and close together (Fig. 3a). The water cooling of the bottom of the sample was quantified by the C1 spot. Thus, the CRI10 (C1) measurement corresponded to the equilibrium research between the rock and the water temperature.

The vertical AB profile centred horizontally on the surface of the sample showed that CRI10 increase from bottom to top until reaching a plateau (Fig. 3b). The break-in slope indicated the transition zone between the cooling by water and the natural cooling. The height of the capillary fringe was adjusted using isolines. This limit was represented by the red dashed line in figure 3. The evolution of this height during the different thermal cycles corresponded to changes in the CWUT and thus in the microstructure of the rock. This parameter was used as comparative values between the cycles.

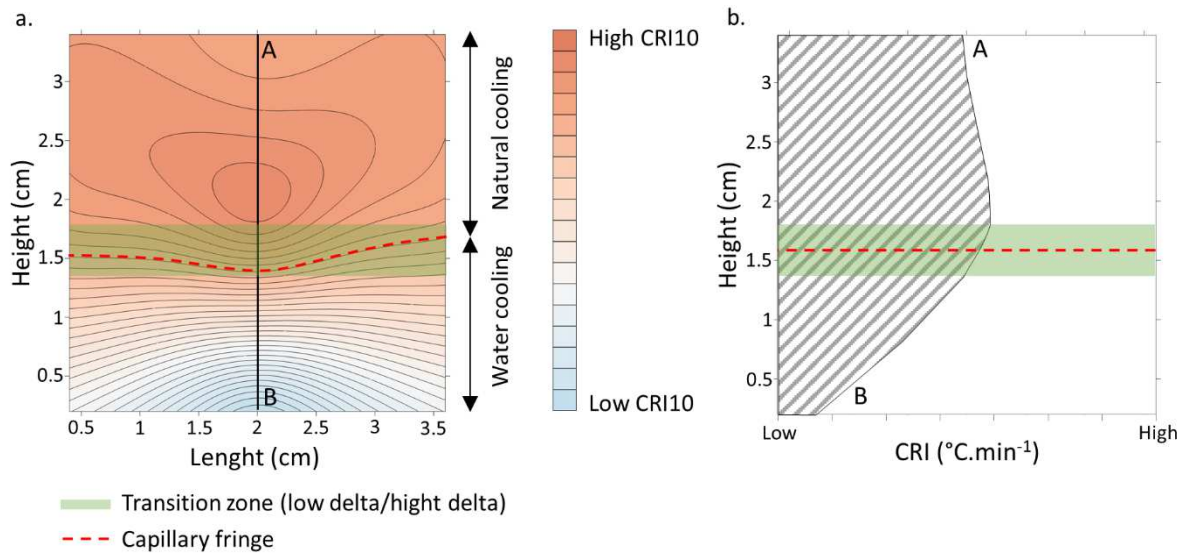

Figure 3: (a) Schematic representation of the cooling rate index (CRI10) on the surface of the samples. (b) CRI10 values along the vertical profile AB. The red dotted line is positioned in the centre of this area. Its position is refined thanks to the isolines on the surface of the sample. Cooling rate index (CRI10) representing the temperature variation per unit of time (10 min).

4_RESULTS

The observations with the naked eye did not reveal any microcracks on the samples after the two treatments. The colour of A, GS, and SM has changed slightly with an accentuation of the reddish tone on the surface, mainly concentrated in the crystal boundaries at 200(5) °C due to the iron oxidation of clays (Vázquez et al., 2016). Clay minerals and phyllosilicates are more sensitive to heat and can be destabilised and undergo several transformations at high-temperatures (Hajpál and Török, 2004). Figure 4 shows the samples before and after EXP2.

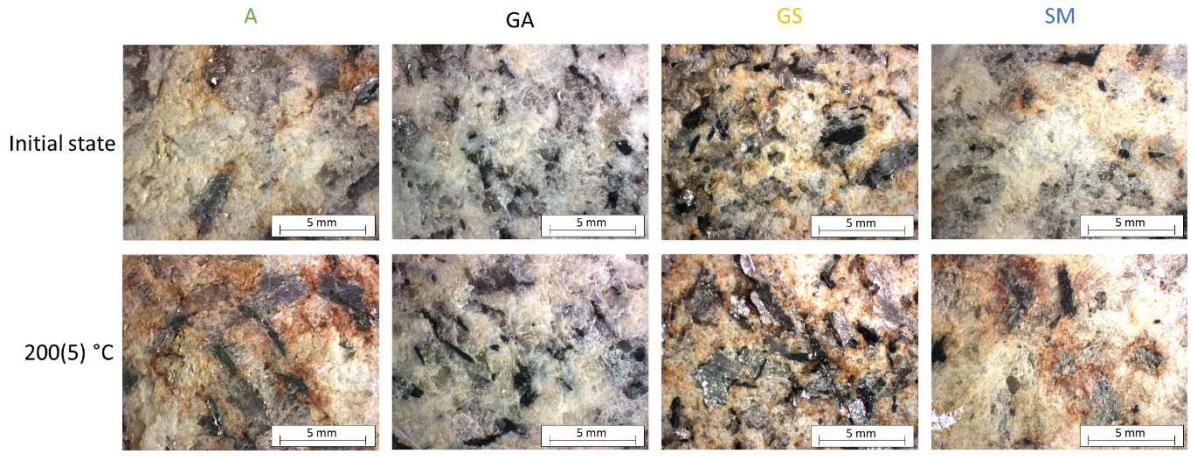

Figure 4: Sample surfaces before and after 5 cycles of heat treatment of EXP2. Albero (A);

Gris Alba (GA); Golden Ski (GS); Silvestre Moreno (SM). Initially, the yellow-brown colour is due to feldspar weathering to clay minerals. A red colour change at crystal boundaries was observed at 200(5) °C due to the iron oxidation of those clays.

4.1 Microstructural analysis

4.1.1 Mercury intrusion porosimetry (MIP)

The analysis was carried out on the 4 granites before heat treatment and after each cycle of EXP1 (90, 100, 110, 120, and 130 °C) as well as for the first and last cycle of the EXP2 (200(1) °C and 200(5) °C). The porosity (%) measured by MIP of the samples after EXP1 and EXP2 are shown in table 3.

Table 3: Total porosity determined by MIP (%) of the 4 granites before and after treatment at different temperatures. Underlined values mean lower values than the fresh rock, in bold the higher values and bold red the first higher value stated as the microcracking threshold.

		EXP1					EXP2	
	Initial state	Cycle 1 90 °C	Cycle 2 100 °C	Cycle 3 110 °C	Cycle 4 120 °C	Cycle 5 130 °C	Cycle 1 200(1) °C	Cycle 5 200(5) °C
A	5.43	5.03	4.72	4.81	3.76	**5.58**	5.15	**6.56**
GA	1.05	0.87	0.95	0.96	0.95	0.80	**1.59**	**1.39**
GS	3.77	3.19	3.08	3.68	**3.93**	3.42	**3.97**	3.56
SM	1.97	**2.30**	**1.98**	**2.44**	**2.25**	**2.01**	**2.12**	**2.16**

Through EXP1, three of the granites (A, GA, GS) experienced firstly a decrease in porosity. Three values (in bold red), at 130 °C for A, 120 °C for GS, and 90 °C for SM were higher than the initial porosity and the preceding value. GA had not shown any increase in its porosity during EXP1.

Through EXP2, the general behaviour was an increase in porosity with high-temperatures, although value fluctuations indicated that crystal and microcracks adjustment was still taking place.

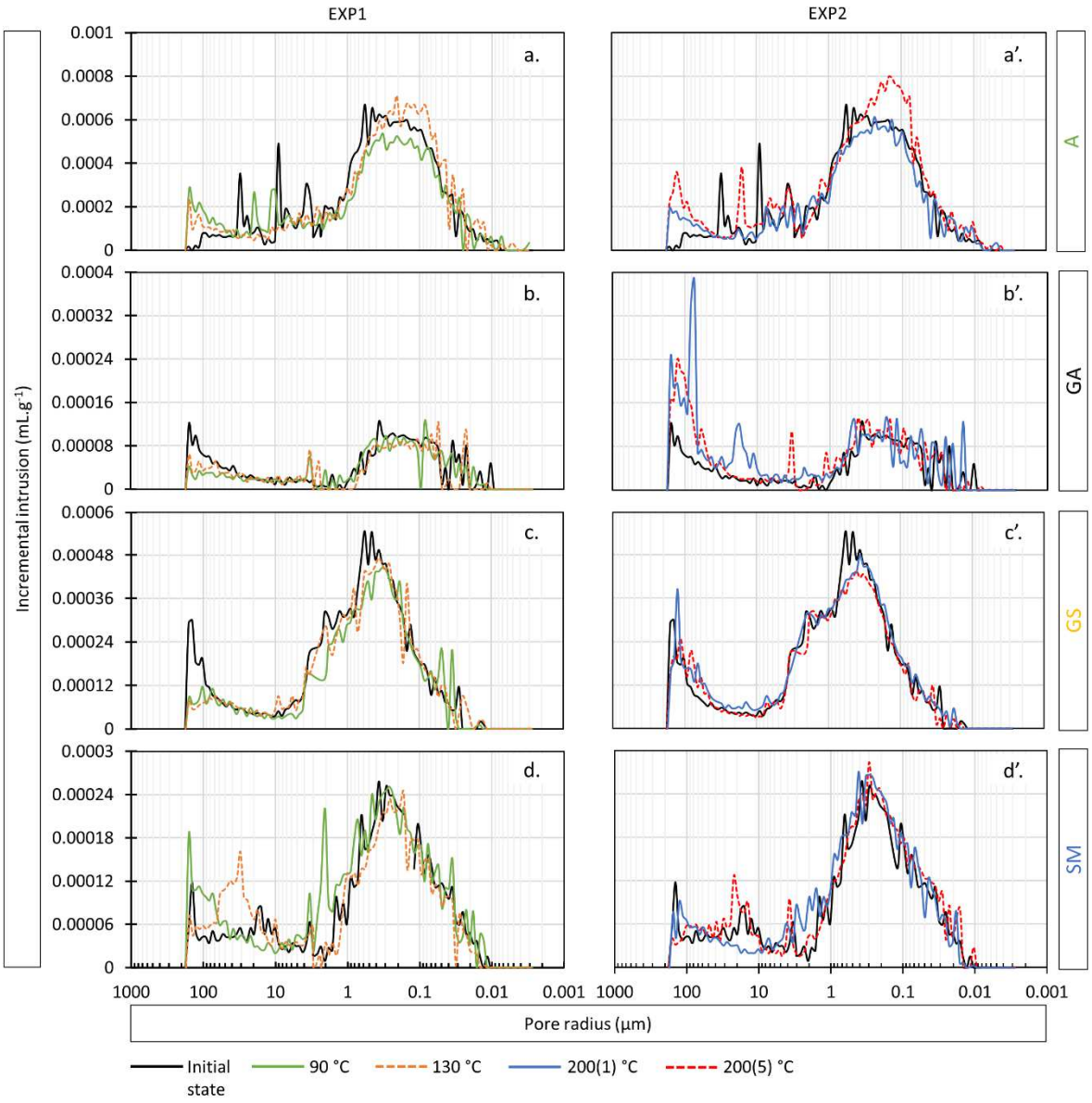

Figure 5: Pore access size distribution curves for EXP1 and EXP2. The curves show the granites tested at room temperature (initial state), 90 °C, 130 °C, 200(1) °C and 200(5) °C. (a-a') Albero, (b-b'), Gris Alba, (c-c') Golden Ski, (d-d') Silvestre Moreno.

The initial MIP curves of the four granites (Fig. 5) can be divided into two parts: i) a main distribution between approximately 0.01 µm and 1-10 µm with unimodal shape; ii) and a heterogeneous distribution of the higher pore radii access.

EXP1:

A showed a main pore distribution in the range of 0.007 to 3 µm (Fig. 5a). The other well-defined subfamily with a heterogeneous distribution showing peaks at 5 and 31 µm. There were variations between MIP yield curves for samples at the initial state and stressed at 90

°C and 130 °C. The main part of the curve showed a volume diminution at 90 °C then recovery at 130 °C. The heterogeneous peaks found at greater pore sizes vanished after heating.

GA is the lowest porous material. The main family curve is observed between 0.01 and 1 µm with the value of higher intensity at 0.4 µm (Fig. 5b). The second family corresponded to a pore access radius from 31 to 157 µm. The pore peak of the last family (about 100 µm) decreased from the first cycle. The last cycle was marked by the apparition of a threshold family around 1-3 µm. The porous volume associated with the mean threshold family slightly decreased with temperature and redistribution of peaks for values under 0.1 µm took place.

GS had a mean threshold family between 0.01 and 10 µm and a heterogeneous family with a mode at 143 µm (Fig. 5c). The curve of the sample heated to 90 °C exhibited a volume reduction for the threshold between 0.2 and 3 µm, slightly recovered at 130 °C. Furthermore, the large decrease of the pore volume associated with high pore radius sizes was observed from the first heating cycle.

SM showed its main pore family dispersed between about 0.01 and 2 µm (Fig. 5d). An increase in porosity at 90 °C was marked by the appearance of a peak centred at 2 µm radius and a gradual increase of the pore volume thereof. At 130 °C, the main distribution did not differ from fresh results, while the pore volume accessible through threshold in the range 10-100 µm increases.

EXP2:

For A, the first episode of heating at 200 °C (200(1) °C) induced a general reduction of the pore volume distributed through all the curve, although a redistribution was observed in pores greater than 34 µm (Fig. 5a'). At the end of EXP2, A showed an increase in porosity of 21% (up to 6.56%). On pores with an access radius greater than 1 µm, the shift of some peaks and the volume increase towards a larger radius (110 µm) indicated a widening of the microcracks during the fifth heating cycle (200(5) °C).

For GA, a development of heterogeneities with heating was observed in the main threshold family (Fig. 5b'). After the first cycle at 200 °C, significant pore radius microcracks formation centred at 18 and 74 µm appeared, the latter softened during the fifth heating cycle. It was

mainly the large accesses of the distribution that were concerned. Porosity values were in agreement with this increase.

For GS, there was a decrease in the main area family, between 0.4 and 0.7 µm at 200(1) °C and between 0.2 and 0.7 µm at 200(5) °C (Fig. 5c'). At 200(1) °C, a peak between 6 and 126 µm was formed and then softened at 200(5) °C.

For SM, the distribution was very irregular over the entire pore radius range after the first heating cycle, then returned to close to the initial state at the end of the test (Fig. 5d'). The porosity volume only increased slightly, also according to the curve variations.

4.1.2 Optical polarising microscopy (POL) and scanning electron microscopy (SEM)

The pre-existing microcracks present naturally in the granites were enhanced by the thermal effects. The observation and comparison of the microscopic images of the fresh and the heated up to 130 °C granites revealed little change, while at 200(1) °C, the variations were slight although evident enough for description. Figure 6 shows microscopy images (POL and SEM) of fresh and thermally damaged granite, 200(1) °C.

After heating, each mineral reacts differently to heat treatment. Thus, new-formed microcracks were observed on the surface of quartz crystals in A but especially in the less weathered granites GA and SM. Mica sheets were slightly raised due to thermal expansion and exhibited microcracking and a higher relief in GA and GS. Mineral particles were detached on the surface of the alkali feldspar crystals in SM.

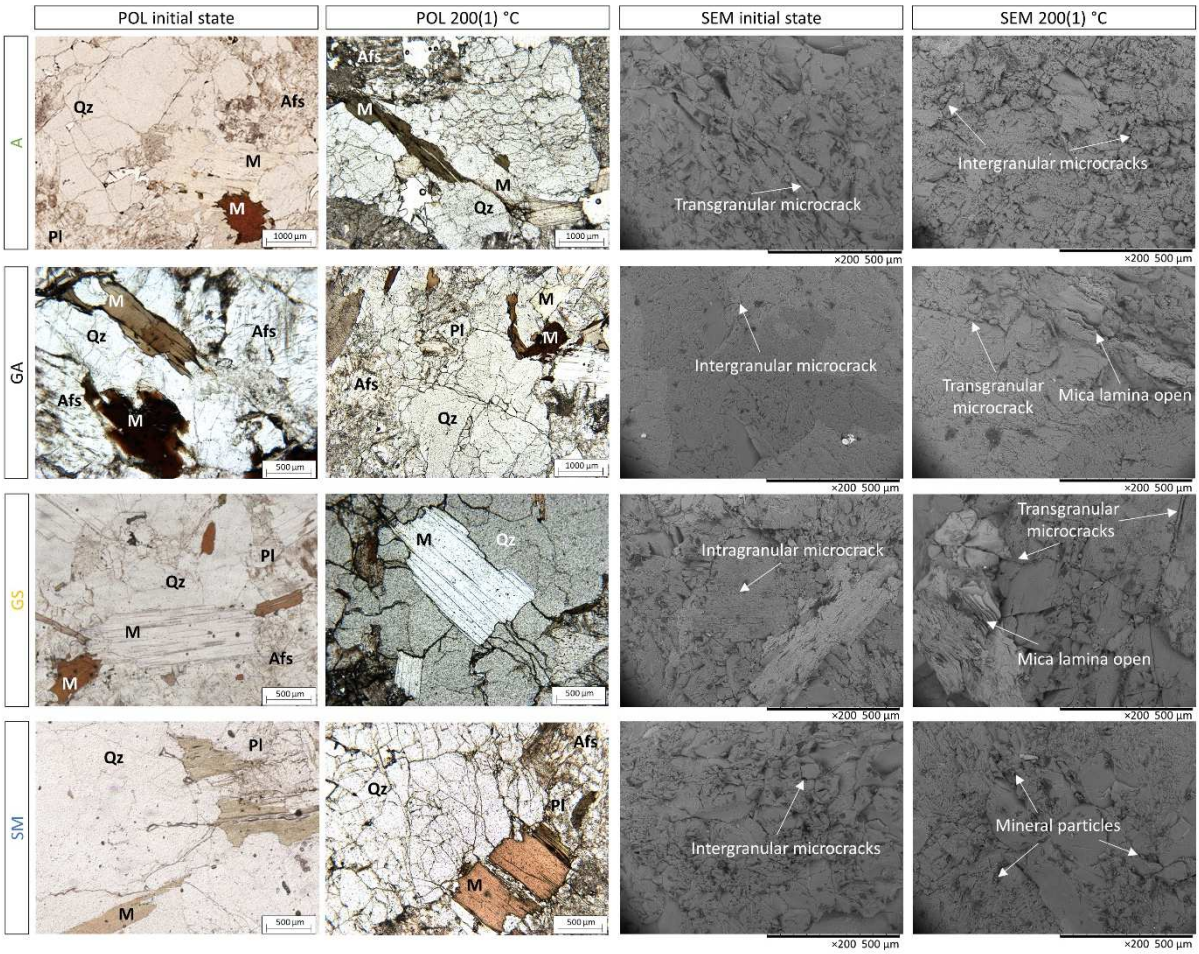

Figure 6: Optical polarising microscopy (POL) and scanning electron microscopy (SEM) illustrating the mineralogy (Qz: quartz; Afs: alkali feldspar; Pl: plagioclase; M: mica) and the microcracking of the four granites before and after one thermal treatment at 200 °C (200(1) °C). Albero (A), Gris Alba (GA), Golden Ski (GS), and Silvestre Moreno (SM).

For A, the heated samples (200(1) °C) showed a crystal surface with a rougher appearance in SEM observations. Intragranular microcracks were already present in the quartz crystals and clearly developed when compared to the POL observations of a heated and fresh rock. The mica presented a slight opening. Microcracks had an average aperture of more than 10 µm after heating and did not present any particular orientation.

For GA, before the thermal treatment, the POL observations showed predominantly an intergranular microcracks network. The POL observations at 200(1) °C showed an increase of intergranular microcracks between the Afs-Pl limit, thus propagating microcracking along the boundaries of adjacent crystals. Notable intragranular microcracks were also present in quartz and alkali feldspar crystals. After one cycle at 200 °C, the pre-existing microcracks became larger and slightly wider in diameter in SEM observations. Some intergranular

microcracks are connected to long transgranular microcracks. The thermal expansion led to visible damage to the GA structure, especially on mica which had an increase in their roughness.

For GS, the POL observations showed a slight opening of mica. The SEM observations revealed that GS was marked by an initial alteration with a visible transgranular microcracking. This granite had pores larger than 30 µm in diameter. After heating, many new microcracks had appeared especially in quartz crystals. Cleavage of mica was also altered, showing irregularities.

For SM, after treatment, the POL observations showed the development of an intragranular microcracking through quartz crystals as well as the advanced deterioration of mica. SM exhibited great diversity in the size and nature of the microcracks. There was also a detachment of microparticles on the surface of the pre-fractured sample at 200(1) °C.

4.1.3 Capillary coefficient (C)

The curves of figure 7 represent the evolution of the capillary coefficient (C) concerning the cycles of the 2 experiments.

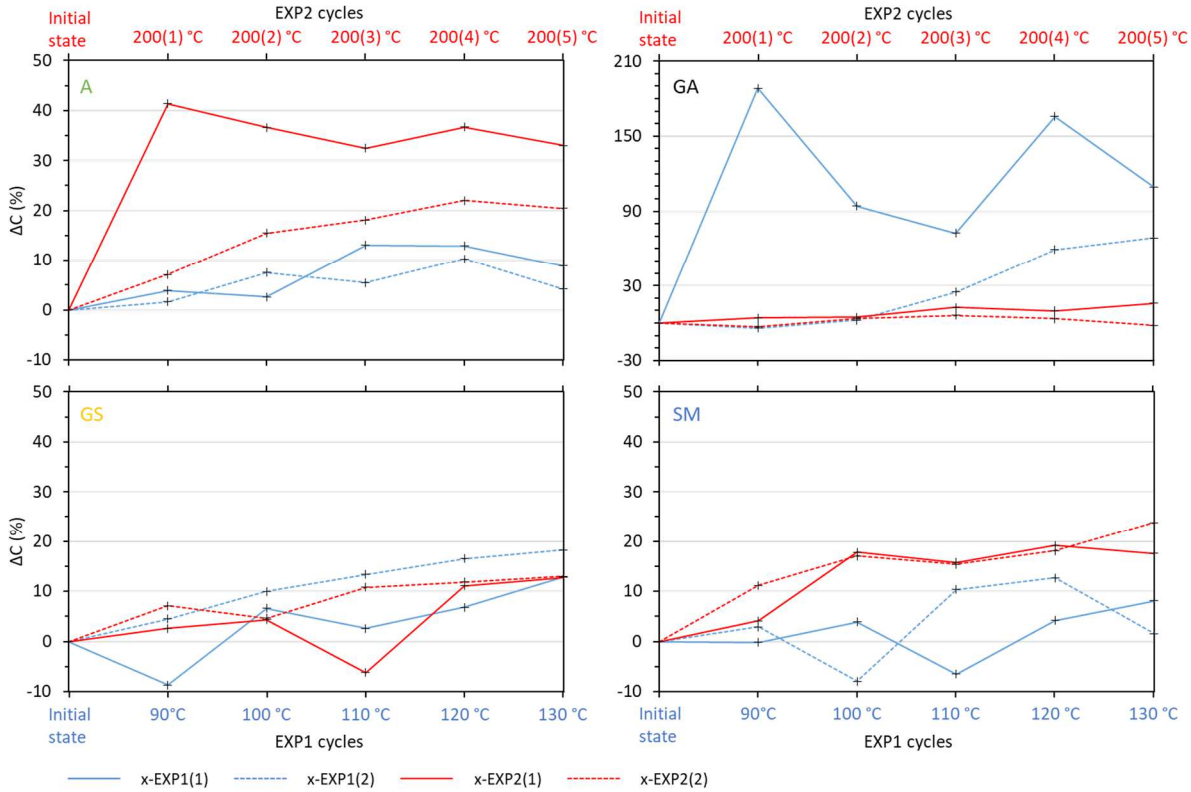

Figure 7: Evolution of the capillary coefficient (C) during the 2 heat treatments (EXP1 in blue and EXP2 in red). The full line corresponds to sample 1 and the dotted line to sample 2.

In general, for both experiments, the coefficient C increased with the thermal cycles. For A-EXP2(1) and GA-EXP1(1), the evolution was non-linear, influenced by a large variation during the first heating cycle. The redistribution of microcracks during the different experiments was noticeable by the non-linear variations of the coefficient C during cycles: some isolated low values and large variability of values between samples of the same granite. The initial heterogeneity of the sample may explain the differences between the acquired data.

EXP1:

Overall, the samples experienced an increase in their coefficients C after heating. For A, the initial coefficients C of the two samples A-EXP1(1) and A-EXP1(2) were 24.9 and 20.1 $g.m^{-2}.s^{-1/2}$ respectively. At, 90 °C the variation was not very evident. The maximum values were reached at 110 °C for sample A-EXP1 (1) with a coefficients C of 28.2 $g.m^{-2}.s^{-½}$ and at 120 °C for the other (A-EXP1 (2)) with a coefficient C of 22.2 $g.m^{-2}.s^{-½}$.

For GA, the initial coefficients C of the two samples GA-EXP1(1) and GA-EXP1(2) were 1.8 and 2.1 $g.m^{-2}.s^{-1/2}$ respectively. This unaltered granite had the highest variability of coefficients C during the cycles. The increase was high from the first cycle for the first sample (GA-EXP(1)) with a coefficients C of 5.08 $g.m^{-2}.s^{-½}$, while the C increase was gradual up to 130 °C for the second sample GA-EXP(2) up to 3.67 $g.m^{-2}.s^{-½}$ at the end of the treatment.

For GS, the initial coefficients C of the two samples GS-EXP1(1) and GS-EXP1(2) were 21.9 and 19.0 $g.m^{-2}.s^{-1/2}$ respectively. At 90 °C, there was a decrease for GS-EXP1(1) and no important change for the GS-EXP1(2). The maximum value was observed at 130 °C with values of 24.7 and 22.6 $g.m^{-2}.s^{-½}$ for GS-EXP1(1) and GS-EXP1(2) respectively.

For SM, the initial coefficients C of the two samples SM-EXP1(1) and SM-EXP1(2) were 9.7 and 10.7 $g.m^{-2}.s^{-1/2}$ respectively. The trends in this granite with the increasing temperature were irregular, with a sharp decrease at 110 °C for SM-EXP1(1) and at 100 °C for the second one. The maximal coefficients C was observed at 130 °C and 120 °C with values of 10.5 and 10.8 $g.m^{-2}. s^{-½}$ for SM-EXP1(1) and SM-EXP1(2), respectively.

EXP2:

The general trends after this test were a gradual increase in the C coefficient.

For A, an increase of C was measured on both samples. The first sample (A-EXP2(1)) increased after the first cycle from 13.2 to 18.7 $g.m^{-2}.s^{-½}$ then nearly stabilised over the other four cycles. The coefficient C of the second sample (A-EXP2(2)) gradually increased until the fifth cycle (200(5) °C) from 21.0 to 25.3 $g.m^{-2}.s^{-½}$.

For GA, the overall trend was an augmentation up to the third cycle (200(3) °C). The coefficients C gained from 4.8 to 5.4 $g.m^{-2}.s^{-½}$ for GA-EXP2(1) while it remained without variation for the other sample.

For GS, the capillary absorption of both samples changed similarly, except for the decrease in GS-EXP2(1) in the third cycle (200(3) °C). Both samples showed a final increase of the same magnitude compared to their initial state.

For SM, the two samples showed a notable increase either during the first or second cycle. The coefficients C then remained stable around 13-14 $g.m^{-2}.s^{-½}$ until the last cycle.

4.2 Infrared thermography (IRT) monitoring of sample cooling

In EXP2, the CRI10 evolution of the air cooling was measured at the level of the control spot 5 (C5) and the water cooling at the level of control spot 1 (C1) (Fig. 2 and 8). The changes of CRI10 values were not linear through the cycles. However, the main trend revealed clearly a strong decrease of the CRI10 in A and a slight one in GS, while GA and SM experimented an increase.

The initial values of CRI10 (C5) were 0.76 $°C.min^{-1}$ for A and 0.82 $°C.min^{-1}$ for GS. GA and SM have intermediate values of 0.77 $°C.min^{-1}$ and 0.78 $°C.min^{-1}$, respectively. The initial CRI10 (C1) was lower in the low porosity GA and SM (0.25 $°C.min^{-1}$) and higher in the high porosity A and GS (0.42 $°C.min^{-1}$).

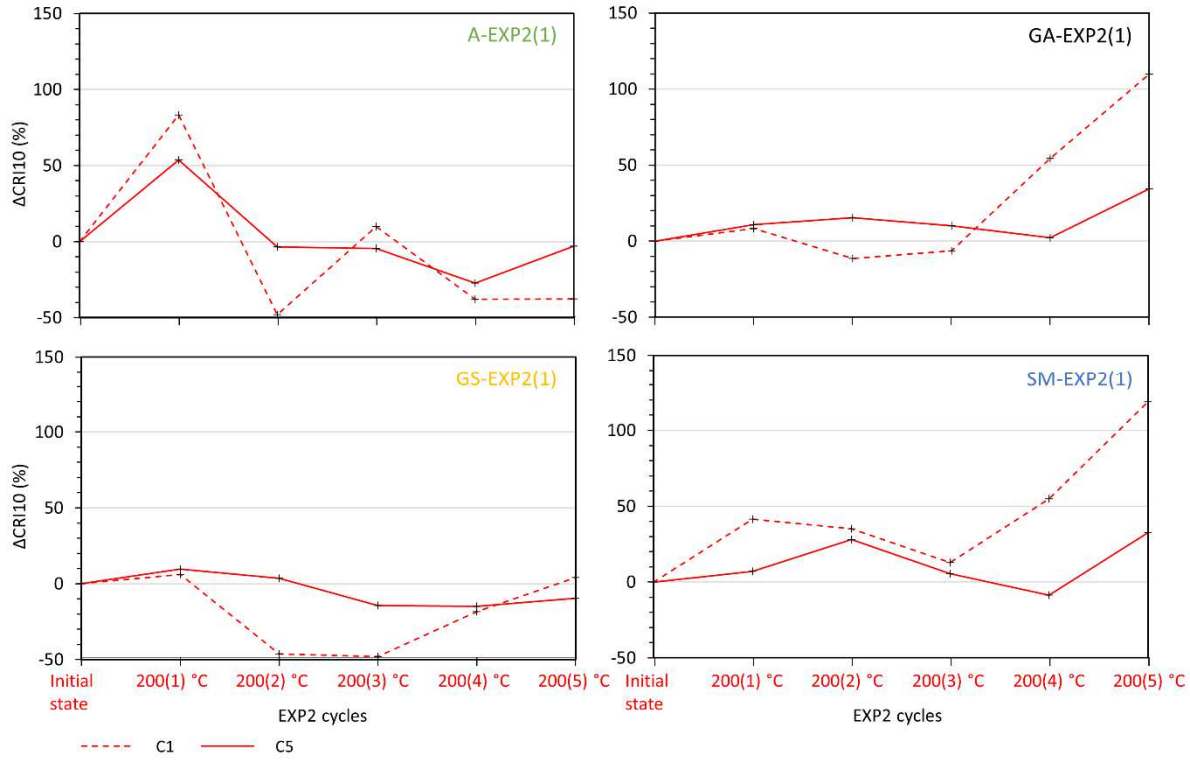

Figure 8: Evolution of the CRI10 measured at the top of the sample (air cooling-spot C5) and the bottom (water cooling-spot C1) through EXP2.

For A, the values through the cycles were the most heterogeneous. It was observed that the air cooling (C5) accelerated from the first heating cycle with an increase of about 50% to the value of 1.17 °C.min^{-1}. The CRI10 measured in the lower part of the sample (C1) also identified an increase of about 80% and reached a value of 0.76 °C.min^{-1}. The following cycle showed a return to the original values of the CRI10 cooled down by air (C5) although there was a decrease of about 30% for the cycle at 200(4) °C. Water cooling showed a decrease to 0.22 °C.min^{-1} in the cycle 200 (2) °C, returns to the origin in the 200(3) °C cycle, and a decrease to 0.26 °C.min^{-1} (about 40%) in the last 2 cycles.

For GA, the final state showed a clear progression compared to the initial state. Whether for the top or the bottom of the sample, the CRI10 did not exceed variations of 15% during the first three cycles. The air cooling that took place at the top of the sample increased by about 30% with a final value of 1.03 °C.min^{-1}. It was during the fourth cycle that the water cooling increased to 0.39 °C.min^{-1} and during the last cycle, the CRI10 was twice its initial value with a value of 0.53 °C.min^{-1}.

For GS, variations in the air cooling were small. The most important changes were identified from cycle 3 marked by a decrease of about 10-15%. Water cooling decreased by about 50% (0.22 °C.min^{-1}) in cycle 2 and 3 and by 20% (0.34 °C.min^{-1}) in cycle 4.

For SM, air cooling increased in cycle 2 and 5, with an increase of 30%. The CRI10 in the lower part (C1) showed an increase of more than twice the initial value up to 0.55 °C.min^{-1} in the last cycle.

The mapping of the CRI10 distribution on the sample surface showed the air-water cooling contrast that was allowed to detect the capillary fringe. The example of GA is shown in figure 9 in which a clear elevation of the capillary fringe was measured through the cycles. For the other granites, the change in the height of the capillary fringe (H) during EXP2 is shown in figure 10.

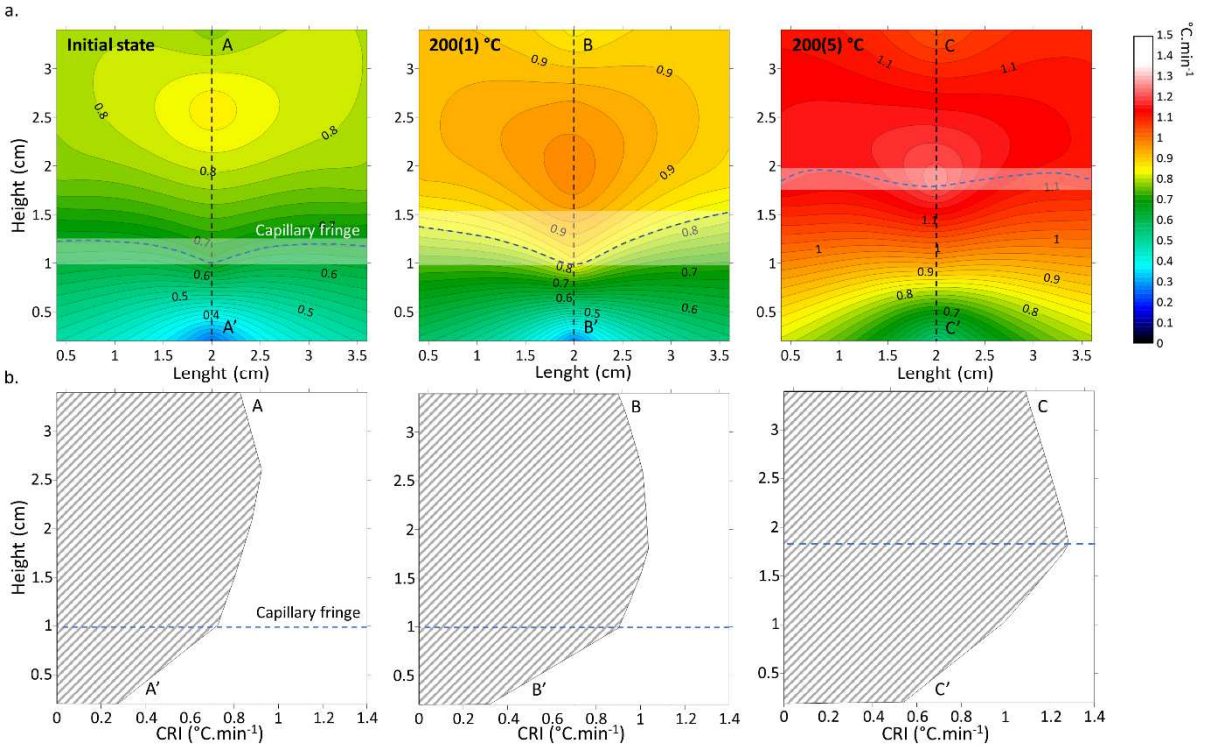

Figure 9: Example of CRI10 mapping (a) and associated profiles (b) obtained by infrared thermography (IRT) monitoring on GA before and after one thermal cycle at 200 °C (200(1) °C) and five thermal cycles (200(5) °C): the dot blue line corresponds to the transition zone and is assumed to correspond to the position of the capillary fringe.

Before the thermal treatment, the capillary height of A was about 1.8 cm. For GA, this height was about 1 cm while GS and SM were in between.

A was marked by a general decreasing trend while for GA, the capillary fringe showed a gradual rise from approximately 1.0 cm to 1.8 cm after the last cycle. For SM and GS, the height of the fringe showed little variation and remained stable.

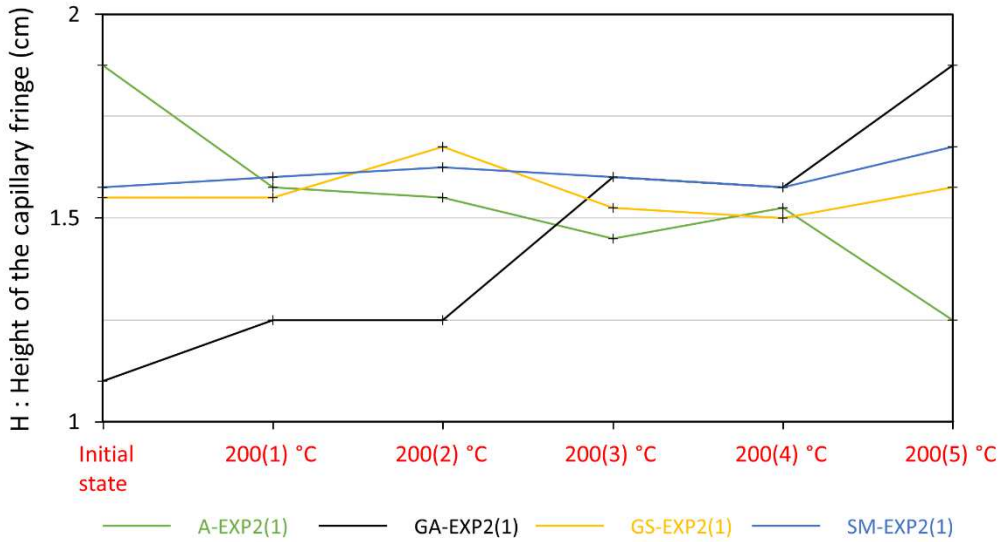

Figure 10: Height of the capillary fringe after the first 10 minutes (H) of capillary absorption of the four granites before and after thermal cycles at 200 °C (EXP2).

5_DISCUSSION

The exposition of granitic rocks to high-temperatures causes an expansion of the rock-forming minerals and a microcrack development above a specific temperature threshold (Argandoña et al., 1985; Géraud et al., 1992; Gómez-Heras et al., 2006; Menéndez et al., 1999). This thermal behaviour depends mainly on two factors, mineralogy and porosity (Benavente et al., 2006; Freire-Lista et al., 2016; Houpert and Homand-Etienne, 1986; Miskovsky et al., 2004). Many researchers agree that the microcrack thermal threshold of granitoids often begins at a temperature of around 100-200 °C (tab. 4).

Table 4: Some previous researches on the thermal microcracking threshold.

Author	Granite	Porosity (%)	Threshold (°C)
(Chen et al., 2017b)	Fujian Province (China)	-	200-400
(Darot et al., 1992)	La Peyratte (France)	-	125
(Argandoña et al., 1985)	Gondomar granodiorite (Spain)	1.37	110-115
(Dwivedi et al., 2008)	Indian granite	0.8	65
(Fan et al., 2017)	Zhejiang Province (China)	-	200-400
(Gautam et al., 2018)	Jalore granite (India)	0.115	300

(Géraud et al., 1992)	Massif de la Borne-Pyrénées-Vendée (France)	0.48-2.3	50-200
(Guo et al., 2018)	Granodianite (China)	1.32	120-150
(Homand-Etienne and Houpert, 1989)	Senones and Remiremont granite (France)	-	200-400
(Jansen et al., 1993)	Lac du Bonnet Granite (Canada)	0.24	80
(Jin et al., 2019)	Shandong province (China)	-	400-500
(Kumari et al., 2017)	Strathbogie batholith (Australia)	1.16	400
(Lin, 2002)	Inada granite (Japan)	0.75	100-125
(Liu and Xu, 2014)	Qinling granite (China)	-	100-200
(Meredith and Atkinson, 1985)	Westerly granite (New England)	1	100-200
(Shao et al., 2015)	Strathbogie granite (Australia)	0.463	200-400
(Singh et al., 2015)	Bundelkhand granite (India)	-	400
(Sun et al., 2015)	Jining, Shandong (China)	0.88	300-400
(Takarli and Prince-Agbodjan, 2008)	-	0.68	105-200
(Yang et al., 2017)	Shandong province (China)	0.828	300-400
(Yin et al., 2015)	Laurentian granite (Canada)	0.64	100-250
(Yu et al., 2015)	Dandong Liaoning Province (China)	-	100
(Zhao and Feng, 2019)	Lu gray granite (China)	-	200-300

Before reaching the thermal threshold, the rock experimented a pore redistribution, defined by an opening and closing of the pre-existent microcracks or the development of new ones. (Géraud et al., 1992) observed the opening of pre-existent biotite and quartz boundaries between 50 and 100 °C. New microcracks were found between 60 °C and 90 °C by Guo et al. (2018) and Jansen et al. (1993) showed microcracking in their granite at temperatures above 80 °C. Dwivedi et al. (2008) observed pre-existing microcracks widening at 65 °C, followed by a closure at temperatures between 100 °C and 125 °C. Lin (2002) observed a microcracks widening threshold at temperatures between 100 °C and 125 °C. Most of the studies found a thermal threshold from 100 °C (Argandoña et al., 1985; Yu et al., 2015). Takarli and Prince-Agbodjan (2008), suggested an increase of microcracking from 105 and 200 °C, according to also to many studies indicating that the critical temperature of granite microcracking takes place at higher temperatures, between 200 and 300 °C (Meredith and Atkinson, 1985; Sun et al., 2015; Yin et al., 2015).

Thermal fatigue is an important failure mechanism in granites. Freire-Lista et al. (2016) and Gómez-Heras et al. (2006) carried out several thermal cycles of continuous heating and cooling up to 105 °C to granitoids and showed that the thermal cyclic effect causes the generation of new microcracks and the fusion of pre-existing ones. Lin (2002) performed 5 to 9 cycles at the same peak temperature (from 200 to 600 °C) and observed that at a

temperature of 200 °C all the microcracks are produced during the first two heating/cooling cycles and from 300 °C thermal microcracking continues developing.

-The effect of mineralogy in granite behaviour

One of the main reasons attributed to the generation of microcracks on poly-mineral rocks is the mismatching of the thermal expansion coefficients of different mineral crystals (Gómez-Heras et al., 2006). The thermal expansion of quartz is anisotropic (a_{11} = 14 × 10^{-6}.K^{-1} and a_{33} = 9 × 10^{-6}.K^{-1}), unlike feldspar with a low and isotropic linear thermal expansion (a_{11} = 4.5 × 10^{-6}.K^{-1} and a_{33} = 4.5 × 10^{-6}.K^{-1}) (Vázquez et al., 2015). Minerals dilate with temperature but sometimes they do not recover the original state after cooling, and the rock shows residual strain.

The linear thermal expansion measurements at 90 °C performed by Vázquez et al. (2015, 2011) on the same granites of this study help to understand the behaviour of these granites during those tests (Fig. 11a). The four studied granites showed a permanent contraction after the first heating-cooling cycle, more notable for the weathered granites A, GS and SM. The direct relation between the Qz/F ratio and the residual strain of granites is shown in figure 11b. Higher quartz content leads to higher residual strain independently of the porosity of the samples.

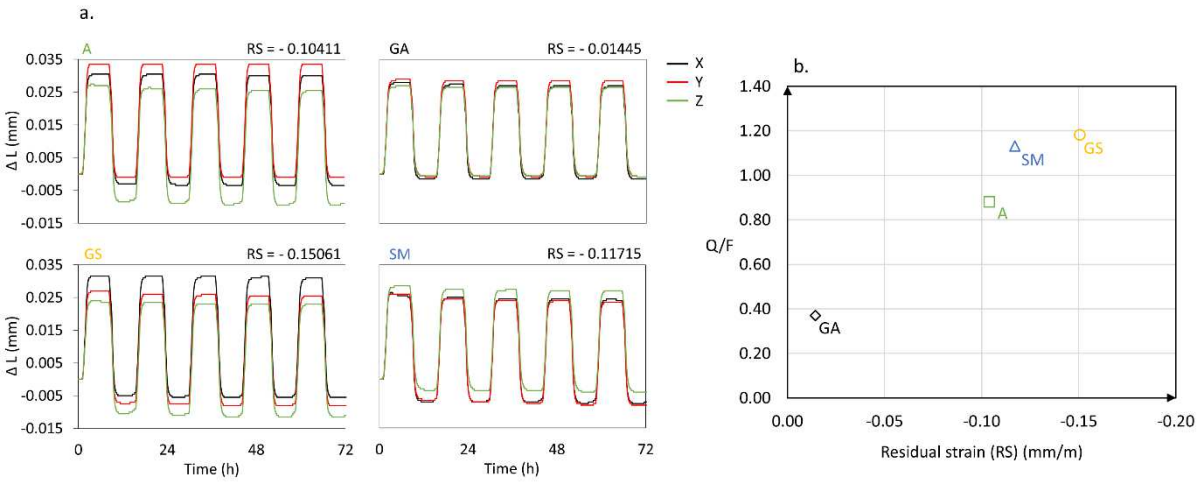

Figure 11: (a) Thermal dilation curve (Δ L) of the four granites submitted to heating-cooling cycles over a range of 20 to 90 °C. Residual strain (RS) expressed in mm/m. (b) Relationship between the Qz/F ratio and average residual strain of A, GA, GS, and SM (Vázquez et al., 2015, 2011, 2010).

-The effect of initial porosity in granite behaviour

The initial porosity and the microcrack density can influence the thermal alteration of the granites. Tuğrul and Zarif (1999) found that the influence of textural characteristics on physical properties seems more important than mineralogy, and Vázquez et al. (2018) stated that only for sound granitoids with porosity under 2%, mineralogical features influence the rock behaviour. The mineral expansion of high porosity rocks intrudes on the voids and reduces the porosity (Géraud et al., 1992). When the rocks are held at the temperature the cracks generated at this temperature remain closed. During cooling, microstructural modifications can appear (Homand-Etienne and Houpert, 1989). If the thermal stress does not reach the microcracks threshold, the minerals will contract during cooling without generating microcracks. If the thermal stress exceeds the cohesion between the grains, the minerals by contracting generate microcracks (Dwivedi et al., 2008). The microcrack geometry (aperture, connection, tortuosity) may play a more important role in the hydric or thermal properties than the porosity volume itself. For this reason, granite detailed study of the pore distribution was carried out from MIP results. The threshold was defined for each granite and the pore access separating the macroporous and microporous domains was defined according to figure 12, at 3 µm for A, 1µm for GA, 10 µm for GS and 2 µm for SM, as mentioned in section 4.1.1. That facilitated to understand in which microcrack size domain the modifications observed in the total porosity took place.

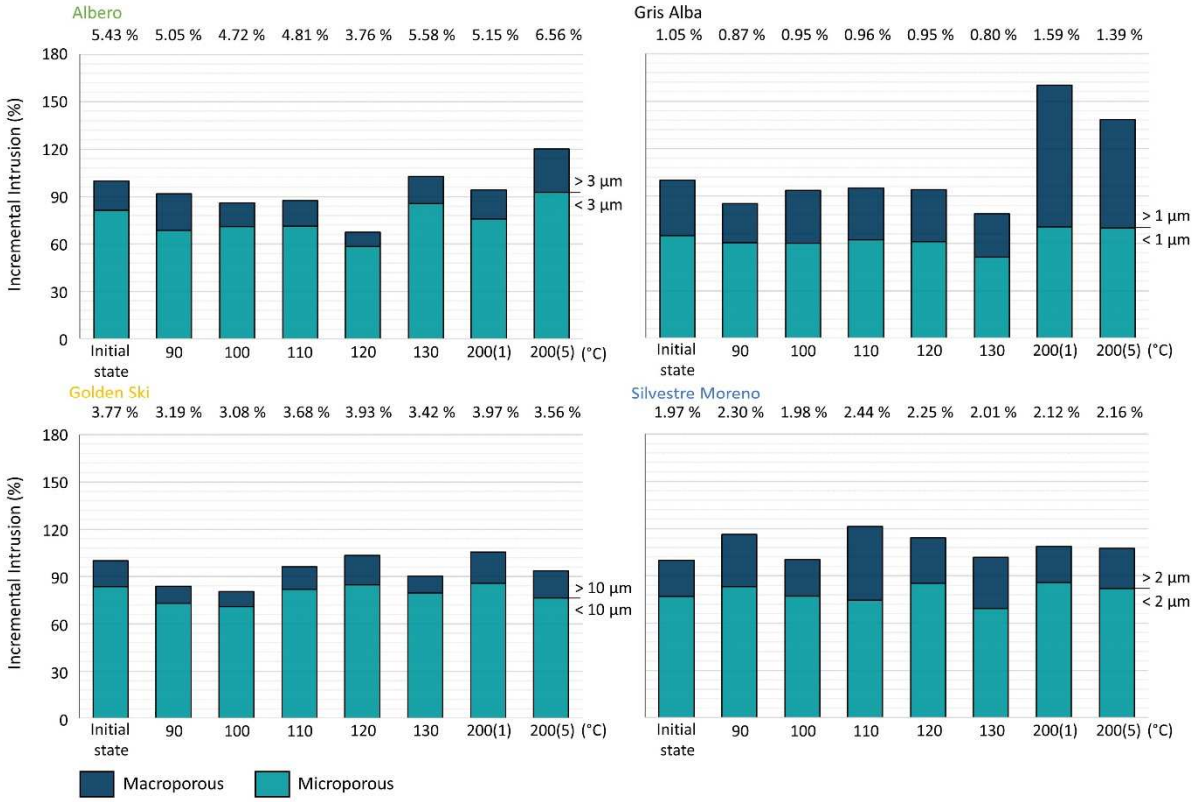

Figure 12: Size distribution of the voids. On the top of each column, the porosity by MIP is detailed.

EXP1: Determination of granite thermal threshold

The low initial porosity of SM within the weathered granites, its high quartz (Qz) and mica content (Vázquez et al., 2015) and its residual strain suggest that the temperature required for a first closure of the pores could be less than 90 °C. Regarding the porosity values (MIP) of table 3, SM is the granite that showed firstly an important increase of porosity considered as a thermal threshold. This occurred at 90 °C and produced mainly an increase in pore access radii over 2 µm (Fig. 12). The capillary coefficient C of the samples varied slightly without a clear trend, although the closure of the pores at 100-110 °C took place that indicated the continuation of the redistribution phase. Beyond these temperatures, the coefficient C increased slightly. Heating to 110-120 °C would mark the new microcrack phase. This conclusion is in agreement with the increase in the connected porosity (> 2 µm) at 110 °C (Fig. 12) that may lead to a more obvious microcracking.

In the second most weathered granite, GS, at 90 °C and 100 °C the total porosity and the radii larger than 10 µm decreased (Fig. 12) in agreement with its residual strain, high Qz/F

612 ratio (Fig. 11) and the variations in the capillary coefficient (Fig. 7). Porosity by MIP indicates
613 that the microcrack threshold was produced at 120 °C although the created space allowed a
614 new closure during the last cycle. Capillary water uptake showed a progressive increase from
615 100 °C that implies the continuous fissuration in the tested samples.

616 The most weathered granite, A, showed contrary results in MIP and capillary coefficient.
617 From the first heating cycle, a porosity around 100 µm appeared, that favouring the
618 progressive increase in water uptake by capillarity. Porosimetry showed a progressive
619 closure up to 120 °C focused on the smaller pores and microcracks that do not affect greatly
620 the capillary forces, explained by the quartz expansion in the existent fissures. A new
621 microcracking was generated at 130 °C in the pore family under 3 µm, so that the
622 temperature range did not allow any pre-existing microcracks widening but possibly
623 increased the open porosity thanks to the connection of previously closed discontinuities.

624 The results of the capillary water uptake tests of GA were not exactly coincident with MIP
625 values. The coefficient C depends not only on the porosity volume but on the width and
626 interconnection between microcracks. The water rises faster when the connections are
627 larger, more numerous, and more uniformly distributed in the sample. MIP showed a
628 microcrack closure through all the test explained by the low Qz/F ratio (Vázquez et al., 2015).
629 The slight expansion of the feldspar occupies the existent fissures and microcracks initially
630 isolated, observed in the intergranular boundaries by microscopic methods, have merged to
631 increase the vertical connections.

632 **EXP2: Effect of thermal fatigue at 200 °C**

633 According to the porosity value change (tab. 3), some rocks experimented a microcracking at
634 200 °C observed under SEM.

635 Granites with lower initial porosity (GA and SM) showed the greatest microcracking increase
636 (Fig. 13), in agreement with Simmons and Cooper (1978). The thermal fatigue in GA and SM
637 leads to a progressive increase of microcracking measured by the different techniques. The
638 damage caused by the first treatment at 200 °C confirmed a pore size augmentation beyond
639 1 µm (Fig. 12) that favoured a faster cooling (CRI). In GA, for the two tested samples, the
640 coefficient C had a positive progression with temperature due to new connections, in

agreement with the increase in the height of the capillary fringe. SM showed good C repeatability for both samples with also a positive progression. The rest of pore-related properties showed an increase, which confirms an increase in microcracking with the thermal cycles.

High porosity and high mica content allowed a mineral expansion and contraction without a catastrophic failure of the rock. Thus, in the case of GS, that despite slight variations through the fatigue cycles, it can be said that the initial and final state of these granites remained similar (Fig. 13). As the number of cycles increased, the porous network of GS has reorganised, avoiding major modifications. The small crystal size and the mica and clay content favoured the mineral adjustment.

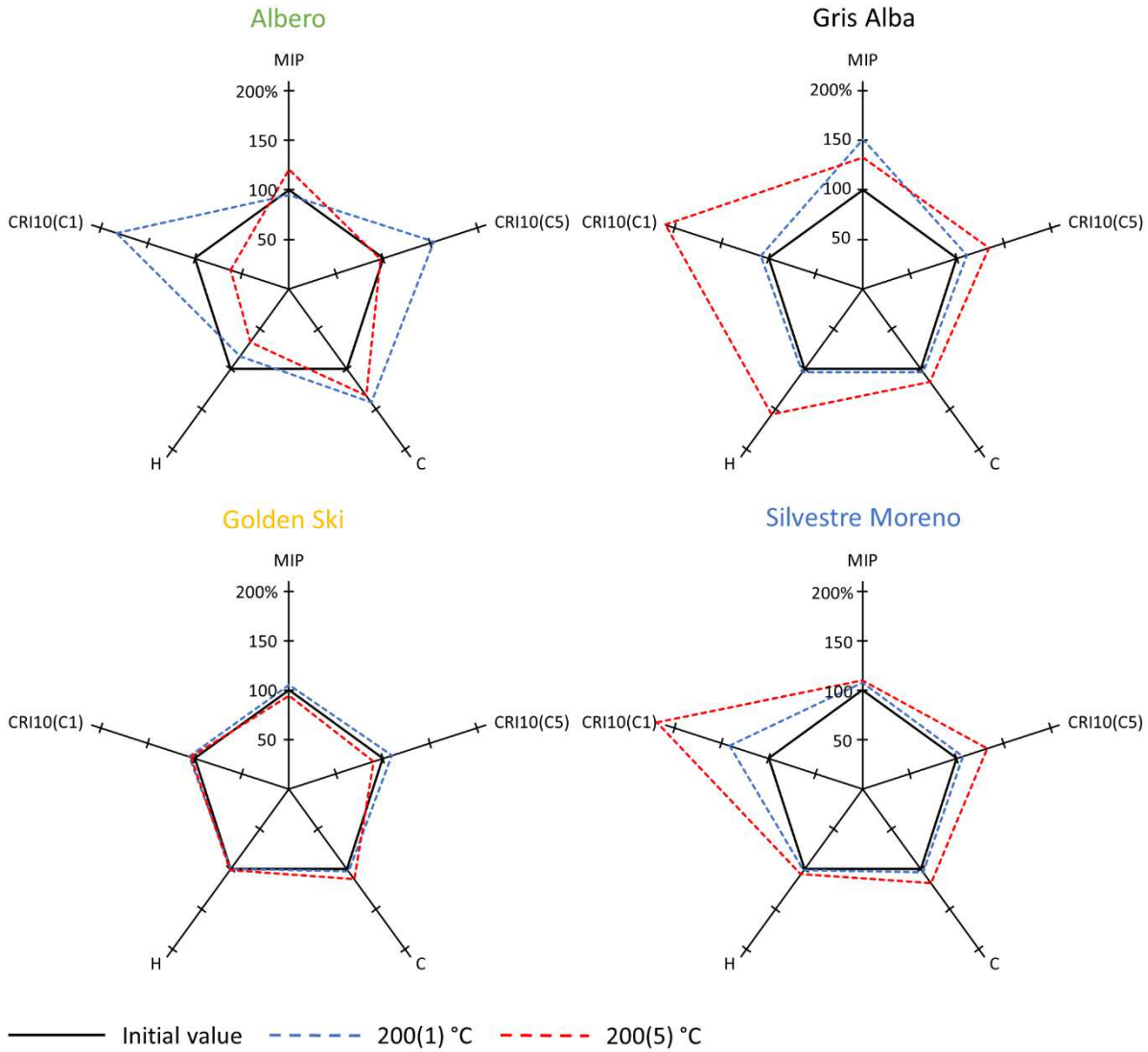

Figure 13: Diagram of the parameter evolution during EXP2: mercury intrusion porosimetry

(MIP), the cooling rate index (CRI10 (C1); CRI10 (C5)) to spot C1 and C5, the capillary coefficient (C) and the height of the capillary fringe detected with an infrared thermography camera (H). Except for MIP, the parameters were measured on the same samples.

A, showed the development of large microcracks that influence the CRI and caused a decrease in the height of the capillary fringe, while MIP remained constant. The capillary coefficient C increased as a result of the widening of the pre-existing intergranular microcracking observed with SEM. After the fatigue test, the bigger microcracks closed possibly by mineral expansion or/and clay remobilisation placed on the edge of pore walls, which did not, however, prevented the continuous circulation of water (Robert, 2004).

6_CONCLUSION

The heterogeneity of low porosity granites induces more dispersed results, while the trends are more similar for high porosity ones. The creation of microcracks and the thermal expansion of minerals are two contradictory phenomena in the evolution of porosity, leading to heterogeneous thermal behaviour. Several parameters are involved in the microcracking evolution with temperature. Thus, for a target temperature, some techniques may indicate an increase in the microcracks while others do not vary or show the contrary. High porosity granites fluctuate between microcracking closure and aperture, with some strong variations that can be considered as a thermal threshold between 90-130 °C. Low porosity granites do not show a thermal threshold at temperatures under 130 °C and only a microcrack closure is measured. However, that is also influenced by the low Qz/F ration of this rock.

Thermal fatigue at a temperature of 200 °C shows the evolution of existent and/or generated microcracks. The lower porosity granites present an evident and progressive microcracking development from the very first heating cycle. Capillary coefficient increases with the repetition of the thermal cycles regardless of the affected pore family. The high porosity granites continue to show a redistribution of pre-existing microcracks through all the test and no signs of new microcracking.

Regarding the studied rocks, porosity shows a stronger impact on the thermal behaviour than the mineralogy. Nevertheless, for similar Qz/F ratios, the lower porosity granites reach the thermal microcracking threshold earlier. Quartz allows to interpret the closure of the

microcracking of granites with high porosity due to its higher thermal expansion. In addition, the low quartz content in the low porosity granite leads to a microcrack closing without microstress development, at low temperature. Mica accommodates the mineral expansion reducing microstresses and the consequent microcracking.

The IRT camera allows to calculate the cooling rate index. Water cooling is more important for granites with high initial porosity. The air cooling remains similar between the different granites. This parameter gives more confident results on the formation of greater microcracks. The image treatment provides a qualitative interpretation of the migration of the capillary fringe. The results show a good correlation with the capillary coefficient, validating this method. These preliminary experiments confirm the utility of the IRT camera in the monitoring of the thermal behaviour of the granites that will help in the field of geothermal energy and nuclear waste storage.

7_REFERENCES

Argandoña, V.G.R.D., Calleja, L., Montoto, M., 1985. Determinación experimental del umbral de microfisuración térmica de la roca matriz o intact rock. Trab. Geol. 15, 299–307. https://doi.org/10.17811/tdg.15.1985.299-307

Bai, B., He, Y., Li, X., 2018. Numerical study on the heat transfer characteristics between supercritical carbon dioxide and granite fracture wall. Geothermics 75, 40–47. https://doi.org/10.1016/j.geothermics.2018.03.002

Benavente, D., Martínez-Martínez, J., Jáuregui, P., Rodríguez, M.A., del Cura, M.A.G., 2006. Assessment of the strength of building rocks using signal processing procedures. Constr. Build. Mater. 20, 562–568. https://doi.org/10.1016/j.conbuildmat.2005.01.043

Berest, P., Vouille, G., 1988. Notions de base de la thermomécanique : La Thermomécanique des Roches. Manuels et Méthodes, Brgm. ed.

Breede, K., Dzebisashvili, K., Liu, X., Falcone, G., 2013. A systematic review of enhanced (or engineered) geothermal systems: past, present and future. Geotherm. Energy 1, 4. https://doi.org/10.1186/2195-9706-1-4

Chaki, S., Takarli, M., Agbodjan, W.P., 2008. Influence of thermal damage on physical properties of a granite rock: Porosity, permeability and ultrasonic wave evolutions. Constr. Build. Mater. 22, 1456–1461. https://doi.org/10.1016/j.conbuildmat.2007.04.002

Chen, G., Wang, J., Li, J., Li, T., Zhang, H., 2018. Influence of Temperature on Crack Initiation and Propagation in Granite. Int. J. Geomech. 18, 04018094. https://doi.org/10.1061/(ASCE)GM.1943-5622.0001182

Chen, S., Yang, C., Wang, G., 2017a. Evolution of thermal damage and permeability of Beishan granite. Appl. Therm. Eng. 110, 1533–1542. https://doi.org/10.1016/j.applthermaleng.2016.09.075

Chen, Y.-L., Wang, S.-R., Ni, J., Azzam, R., Fernández-steeger, T.M., 2017b. An experimental study of the mechanical properties of granite after high temperature exposure based on mineral characteristics. Eng. Geol. 220, 234–242. https://doi.org/10.1016/j.enggeo.2017.02.010

Darot, M., Gueguen, Y., Baratin, M.-L., 1992. Permeability of thermally cracked granite. Geophys. Res. Lett. 19, 869–872. https://doi.org/10.1029/92GL00579

Ding, Q.-L., Ju, F., Mao, X.-B., Ma, D., Yu, B.-Y., Song, S.-B., 2016. Experimental Investigation of the Mechanical Behavior in Unloading Conditions of Sandstone After High-Temperature Treatment. Rock Mech. Rock Eng. 49, 2641–2653. https://doi.org/10.1007/s00603-016-0944-x

Dwivedi, R.D., Goel, R.K., Prasad, V.V.R., Sinha, A., 2008. Thermo-mechanical properties of Indian and other granites. Int. J. Rock Mech. Min. Sci. 45, 303–315. https://doi.org/10.1016/j.ijrmms.2007.05.008

Fan, L.F., Wu, Z.J., Wan, Z., Gao, J.W., 2017. Experimental investigation of thermal effects on dynamic behavior of granite. Appl. Therm. Eng. 125, 94–103. https://doi.org/10.1016/j.applthermaleng.2017.07.007

Farias, P., Gallastegui, G., González Lodeiro, F., Marquínez, J., Martín Parra, L.M., Martínez Catalán, J.R., Pablo Maciá, J. de, Rodríguez Fernández, L.R., 1987. Aportaciones al conocimiento de la litoestratigrafía y estructura de Galicia Central. Mem. Fac. Ciênc. Universidade Porto 1, 411–431.

Freire-Lista, D.M., Fort, R., Varas-Muriel, M.J., 2016. Thermal stress-induced microcracking in building granite. Eng. Geol. 206, 83–93. https://doi.org/10.1016/j.enggeo.2016.03.005

Gautam, P.K., Verma, A.K., Jha, M.K., Sharma, P., Singh, T.N., 2018. Effect of high temperature on physical and mechanical properties of Jalore granite. J. Appl. Geophys. 159, 460–474. https://doi.org/10.1016/j.jappgeo.2018.07.018

Géraud, Y., Mazerolle, F., Raynaud, S., 1992. Comparison between connected and overall porosity of thermally stressed granites. J. Struct. Geol., Mechanical Instabilities in Rocks and Tectonics 14, 981–990. https://doi.org/10.1016/0191-8141(92)90029-V

Gómez-Heras, M., Smith, B.J., Fort, R., 2006. Surface temperature differences between minerals in crystalline rocks: Implications for granular disaggregation of granites through thermal fatigue. Geomorphology 78, 236–249. https://doi.org/10.1016/j.geomorph.2005.12.013

Guo, L.-L., Zhang, Y.-B., Zhang, Y.-J., Yu, Z.-W., Zhang, J.-N., 2018. Experimental investigation of granite properties under different temperatures and pressures and numerical analysis of damage effect in enhanced geothermal system. Renew. Energy 126, 107–125. https://doi.org/10.1016/j.renene.2018.02.117

Hajpál, M., Török, Á., 2004. Mineralogical and colour changes of quartz sandstones by heat. Environ. Geol. 46, 311–322. https://doi.org/10.1007/s00254-004-1034-z

Hammecker, C., Jeannette, D., 1994. Modelling the capillary imbibition kinetics in sedimentary rocks: Role of petrographical features. Transp. Porous Media 17, 285–303. https://doi.org/10.1007/BF00613588

Hammecker, C., Mertz, J.-D., Fischer, C., Jeannette, D., 1993. A geometrical model for numerical simulation of capillary imbibition in sedimentary rocks. Transp. Porous Media 12, 125–141. https://doi.org/10.1007/BF00616976

Heuze, F.E., 1983. High-temperature mechanical, physical and Thermal properties of granitic rocks—A review. Int. J. Rock Mech. Min. Sci. Geomech. Abstr. 20, 3–10. https://doi.org/10.1016/0148-9062(83)91609-1

Hoekmark, H., Faelth, B., 2003. Thermal dimensioning of the deep repository. Influence of canister spacing, canister power, rock thermal properties and nearfield design on the maximum canister surface temperature (No. SKB-TR--03-09). Swedish Nuclear Fuel and Waste Management Co.

Homand-Etienne, F., Houpert, R., 1989. Thermally induced microcracking in granites: characterization and analysis. Int. J. Rock Mech. Min. Sci. Geomech. Abstr. 26, 125–134. https://doi.org/10.1016/0148-9062(89)90001-6

Houpert, R., Homand-Etienne, F., 1986. Données récentes sur le comportement des roches en fonction de la température. P Berest Ph Weber Thermoméc. Roches Man. Méthodes 304–312.

773 Huang, Y.-H., Yang, S.-Q., Tian, W.-L., Zhao, J., Ma, D., Zhang, C.-S., 2017. Physical and mechanical
774 behavior of granite containing pre-existing holes after high temperature treatment. Arch. Civ.
775 Mech. Eng. 17, 912–925. https://doi.org/10.1016/j.acme.2017.03.007
776 Isaka, B.L.A., Gamage, R.P., Rathnaweera, T.D., Perera, M.S.A., Chandrasekharam, D., Kumari, W.G.P.,
777 2018. An Influence of Thermally-Induced Micro-Cracking under Cooling Treatments:
778 Mechanical Characteristics of Australian Granite. Energies 11, 1338.
779 https://doi.org/10.3390/en11061338
780 Jansen, D.P., Carlson, S.R., Young, R.P., Hutchins, D.A., 1993. Ultrasonic imaging and acoustic
781 emission monitoring of thermally induced microcracks in Lac du Bonnet granite. J. Geophys.
782 Res. Solid Earth 98, 22231–22243. https://doi.org/10.1029/93JB01816
783 Jin, P., Hu, Y., Shao, J., Zhao, G., Zhu, X., Li, C., 2019. Influence of different thermal cycling treatments
784 on the physical, mechanical and transport properties of granite. Geothermics 78, 118–128.
785 https://doi.org/10.1016/j.geothermics.2018.12.008
786 Kumari, W.G.P., Ranjith, P.G., Perera, M.S.A., Chen, B.K., Abdulagatov, I.M., 2017. Temperature-
787 dependent mechanical behaviour of Australian Strathbogie granite with different cooling
788 treatments. Eng. Geol. 229, 31–44. https://doi.org/10.1016/j.enggeo.2017.09.012
789 Le Maitre, R.W. (Ed.), 2002. Igneous Rocks: A Classification and Glossary of Terms: Recommendations
790 of the International Union of Geological Sciences Subcommission on the Systematics of
791 Igneous Rocks, 2nd ed. Cambridge University Press, Cambridge.
792 https://doi.org/10.1017/CBO9780511535581
793 Li, B., Ju, F., Xiao, M., Ning, P., 2019. Mechanical stability of granite as thermal energy storage
794 material: An experimental investigation. Eng. Fract. Mech. 211, 61–69.
795 https://doi.org/10.1016/j.engfracmech.2019.02.008
796 Lin, W., 2002. Permanent strain of thermal expansion and thermally induced microcracking in Inada
797 granite. J. Geophys. Res. Solid Earth 107, ECV 3-1. https://doi.org/10.1029/2001JB000648
798 Liu, S., Xu, J., 2014. Mechanical properties of Qinling biotite granite after high temperature
799 treatment. https://doi.org/10.1016/J.IJRMMS.2014.07.008
800 Ludwig, N., Rosina, E., Sansonetti, A., 2018. Evaluation and monitoring of water diffusion into stone
801 porous materials by means of innovative IR thermography techniques. Measurement 118,
802 348–353. https://doi.org/10.1016/j.measurement.2017.09.002
803 Menéndez, B., David, C., Darot, M., 1999. A study of the crack network in thermally and mechanically
804 cracked granite samples using confocal scanning laser microscopy. Phys. Chem. Earth Part
805 Solid Earth Geod. 24, 627–632. https://doi.org/10.1016/S1464-1895(99)00091-5
806 Meredith, P.G., Atkinson, B.K., 1985. Fracture toughness and subcritical crack growth during high-
807 temperature tensile deformation of Westerly granite and Black gabbro. Phys. Earth Planet.
808 Inter. 39, 33–51. https://doi.org/10.1016/0031-9201(85)90113-X
809 Mineo, S., Pappalardo, G., 2016. The Use of Infrared Thermography for Porosity Assessment of Intact
810 Rock. Rock Mech. Rock Eng. 49, 3027–3039. https://doi.org/10.1007/s00603-016-0992-2
811 Miskovsky, K., Duarte, M.T., Kou, S.Q., Lindqvist, P.-A., 2004. Influence of the mineralogical
812 composition and textural properties on the quality of coarse aggregates. J. Mater. Eng.
813 Perform. 13, 144–150. https://doi.org/10.1361/10599490418334
814 NF EN 15801, Conservation of cultural property-Test methods-Determination of water absorption by
815 capillarity, 2010.
816 Olasolo, P., Juárez, M.C., Morales, M.P., D´Amico, S., Liarte, I.A., 2016. Enhanced geothermal systems
817 (EGS): A review. Renew. Sustain. Energy Rev. 56, 133–144.
818 https://doi.org/10.1016/j.rser.2015.11.031
819 Pandey, S.N., Chaudhuri, A., Kelkar, S., 2017. A coupled thermo-hydro-mechanical modeling of
820 fracture aperture alteration and reservoir deformation during heat extraction from a
821 geothermal reservoir. Geothermics 65, 17–31.
822 https://doi.org/10.1016/j.geothermics.2016.08.006

Pappalardo, G., Mineo, S., Zampelli, S.P., Cubito, A., Calcaterra, D., 2016. InfraRed Thermography proposed for the estimation of the Cooling Rate Index in the remote survey of rock masses. Int. J. Rock Mech. Min. Sci. 83, 182–196. https://doi.org/10.1016/j.ijrmms.2016.01.010
Parnell, J., 1988. Migration of biogenic hydrocarbons into granites: a review of hydrocarbons in British plutons. Mar. Pet. Geol. 5, 385–396. https://doi.org/10.1016/0264-8172(88)90032-3
Reuschlé, T., Gbaguidi Haore, S., Darot, M., 2006. The effect of heating on the microstructural evolution of La Peyratte granite deduced from acoustic velocity measurements. Earth Planet. Sci. Lett. 243, 692–700. https://doi.org/10.1016/j.epsl.2006.01.038
Ritter, H.L., Drake, L.C., 1945. Pressure Porosimeter and Determination of Complete Macropore-Size Distributions. Pressure Porosimeter and Determination of Complete Macropore-Size Distributions. Ind. Eng. Chem. Anal. Ed. 17, 782–786. https://doi.org/10.1021/i560148a013
Robert, R., 2004. Analytical characterization of porous geomaterials: reference assessment in some sedimentary rocks (PhD Thesis). PhD thesis, Humboldt University, Berlin.
Roels, S., Carmeliet, J., Hens, H., Elsen, J., 2000. Microscopic analysis of imbibition processes in oolitic limestone. Geophys. Res. Lett. 27, 3533–3536. https://doi.org/10.1029/1999GL008471
Sajid, M., Arif, M., 2015. Reliance of physico-mechanical properties on petrographic characteristics: consequences from the study of Utla granites, north-west Pakistan. Bull. Eng. Geol. Environ. 74, 1321–1330. https://doi.org/10.1007/s10064-014-0690-9
Shao, S., Ranjith, P.G., Wasantha, P.L.P., Chen, B.K., 2015. Experimental and numerical studies on the mechanical behaviour of Australian Strathbogie granite at high temperatures: An application to geothermal energy. Geothermics 54, 96–108. https://doi.org/10.1016/j.geothermics.2014.11.005
Simmons, G., Cooper, H.W., 1978. Thermal cycling cracks in three igneous rocks. Int. J. Rock Mech. Min. Sci. Geomech. Abstr. 15, 145–148. https://doi.org/10.1016/0148-9062(78)91220-2
Singh, B., Ranjith, P.G., Chandrasekharam, D., Viete, D., Singh, H.K., Lashin, A., Al Arifi, N., 2015. Thermo-mechanical properties of Bundelkhand granite near Jhansi, India. Geomech. Geophys. Geo-Energy Geo-Resour. 1, 35–53. https://doi.org/10.1007/s40948-015-0005-z
Sousa, L.M.O., 2013. The influence of the characteristics of quartz and mineral deterioration on the strength of granitic dimensional stones. Environ. Earth Sci. 69, 1333–1346. https://doi.org/10.1007/s12665-012-2036-x
Staněk, M., Géraud, Y., 2019. Granite microporosity changes due to fracturing and alteration: secondary mineral phases as proxies for porosity and permeability estimation. Solid Earth 10, 251–274. https://doi.org/10.5194/se-10-251-2019
Sun, Q., Zhang, W., Xue, L., Zhang, Z., Su, T., 2015. Thermal damage pattern and thresholds of granite. Environ. Earth Sci. 74, 2341–2349. https://doi.org/10.1007/s12665-015-4234-9
Takarli, M., Prince-Agbodjan, W., 2008. Temperature Effects on Physical Properties and Mechanical Behavior of Granite: Experimental Investigation of Material Damage. J. ASTM Int. 5, 1–13. https://doi.org/10.1520/JAI100464
Tang, Z.C., Sun, M., Peng, J., 2019. Influence of high temperature duration on physical, thermal and mechanical properties of a fine-grained marble. Appl. Therm. Eng. 156, 34–50. https://doi.org/10.1016/j.applthermaleng.2019.04.039
Tuğrul, A., Zarif, I.H., 1999. Correlation of mineralogical and textural characteristics with engineering properties of selected granitic rocks from Turkey. Eng. Geol. 51, 303–317. https://doi.org/10.1016/S0013-7952(98)00071-4
Vázquez, P., Acuña, M., Benavente, D., Gibeaux, S., Navarro, I., Gomez-Heras, M., 2016. Evolution of surface properties of ornamental granitoids exposed to high temperatures. Constr. Build. Mater. 104, 263–275. https://doi.org/10.1016/j.conbuildmat.2015.12.051
Vázquez, P., Alonso, F.J., Esbert, R.M., Ordaz, J., 2010. Ornamental granites: Relationships between p-waves velocity, water capillary absorption and the crack network. Constr. Build. Mater., Special Issue on Fracture, Acoustic Emission and NDE in Concrete (KIFA-5) 24, 2536–2541. https://doi.org/10.1016/j.conbuildmat.2010.06.002

874 Vázquez, P., Sánchez-Delgado, N., Carrizo, L., Thomachot-Schneider, C., Alonso, F.J., 2018. Statistical
875 approach of the influence of petrography in mechanical properties and durability of granitic
876 stones. Environ. Earth Sci. 77, 287. https://doi.org/10.1007/s12665-018-7475-6
877 Vázquez, P., Shushakova, V., Gómez-Heras, M., 2015. Influence of mineralogy on granite decay
878 induced by temperature increase: Experimental observations and stress simulation. Eng.
879 Geol. 189, 58–67. https://doi.org/10.1016/j.enggeo.2015.01.026
880 Vázquez, P., Siegesmund, S., Alonso, F.J., 2011. Bowing of dimensional granitic stones. Environ. Earth
881 Sci. 63, 1603–1612. https://doi.org/10.1007/s12665-010-0882-y
882 Vera, J.A., 2004. Geología de España. SGE-IGME.
883 Witherspoon, P.A., Nelson, P., Doe, T., Thorpe, R., Paulsson, B., Gale, J., Forster, C., 1980. Rock Mass
884 Characterization for Storage of Nuclear Waste in Granite. IEEE Trans. Nucl. Sci. 27, 1280–
885 1290. https://doi.org/10.1109/TNS.1980.4331008
886 Yang, S.-Q., Ranjith, P.G., Jing, H.-W., Tian, W.-L., Ju, Y., 2017. An experimental investigation on
887 thermal damage and failure mechanical behavior of granite after exposure to different high
888 temperature treatments. Geothermics 65, 180–197.
889 https://doi.org/10.1016/j.geothermics.2016.09.008
890 Yin, T., Li, X., Cao, W., Xia, K., 2015. Effects of Thermal Treatment on Tensile Strength of Laurentian
891 Granite Using Brazilian Test. Rock Mech. Rock Eng. 48, 2213–2223.
892 https://doi.org/10.1007/s00603-015-0712-3
893 Yu, Q.L., Ranjith, P.G., Liu, H.Y., Yang, T.H., Tang, S.B., Tang, C.A., Yang, S.Q., 2015. A Mesostructure-
894 based Damage Model for Thermal Cracking Analysis and Application in Granite at Elevated
895 Temperatures. Rock Mech. Rock Eng. 48, 2263–2282. https://doi.org/10.1007/s00603-014-
896 0679-5
897 Zhao, P., Feng, Z., 2019. Thermal Deformation of Granite under Different Temperature and Pressure
898 Pathways. Adv. Mater. Sci. Eng. 2019, 7869804. https://doi.org/10.1155/2019/7869804
899